

1 * Preprint uploaded to EarthArxiv. This article is in
2 press with G3. Please cite the published version*

3 **Reconstructing Magma Storage Depths for the 2018**
4 **Kīlauean Eruption from Melt inclusion CO₂ Contents:**
5 **The Importance of Vapor Bubbles**

6 **P. E. Wieser¹, H. Lamadrid², J. Maclennan¹, M. Edmonds¹, S. Matthews³, K.**
7 **Iacovino⁴, F.E. Jenner⁵, C. Gansecki⁶, F. Trusdell⁷, R.L. Lee⁷ and E.**
8 **Ilyinskaya⁸**

9 ¹Department of Earth Sciences, University of Cambridge, UK.

10 ²Geological Sciences, University of Missouri, 65211, US.

11 ³Johns Hopkins University, Department of Earth and Planetary Sciences, Baltimore, MD 21218, USA.

12 ⁴Jacobs, NASA Johnson Space Center, Houston, TX 77058, USA.

13 ⁵School of Environment, Earth and Ecosystem Sciences, The Open University, MK7 6AA, UK

14 ⁶Department of Geology, University of Hawai'i at Hilo, Hilo, HI 96720, USA

15 ⁷USGS Hawaiian Volcano Observatory, Hilo, HI 96720, USA

16 ⁸School of Earth and Environment, University of Leeds, UK

17 **Key Points:**

- 18 • Petrological, gaseous and geophysical observations can be reconciled by a
19 model where Fissure 8 was supplied from two storage reservoirs (~1–2 and
20 3–5 km depth)
- 21 • Extensive post-entrapment crystallization of melt inclusions within High-Fo
22 olivines (Fo>81.5) caused ~90% of the CO₂ to enter the vapor bubble.
- 23 • Raman analyses of vapor bubbles combined with choice of a suitable H₂O-
24 CO₂ solubility model is required to accurately determine magma storage
25 depths.

Corresponding author: P. Wieser, penny.wieser@gmail.com

Abstract

The 2018 lower East Rift Zone (LERZ) eruption and the accompanying collapse of the summit caldera marked the most destructive episode of activity at Kīlauea Volcano in the last 200 years. The eruption was extremely well-monitored, with extensive real-time lava sampling as well as continuous geodetic data capturing the caldera collapse. This multi-parameter dataset provides an exceptional opportunity to determine the reservoir geometry and magma transport paths supplying Kīlauea’s LERZ. The forsterite contents of olivine crystals, together with the degree of major element disequilibrium with carrier melts, indicates that two distinct crystal populations were erupted from Fissure 8 (termed High- and Low-Fo). Melt inclusion entrapment pressures reveal that Low-Fo olivines (close to equilibrium with their carrier melts) crystallized within the Halema’uma’u reservoir (~ 2 km depth), while many High-Fo olivines ($> \text{Fo}_{81.5}$; far from equilibrium with their carrier melts) crystallized within the South Caldera reservoir (~ 3 – 5 km depth). Melt inclusions in High-Fo olivines experienced extensive post-entrapment crystallization following their incorporation into cooler, more evolved melts. This favoured the growth of a CO_2 -rich vapor bubble, containing up to 99% of the total melt inclusion CO_2 budget (median=93%). If this CO_2 -rich bubble is not accounted for, entrapment depths are significantly underestimated. Conversely, reconstructions using equation of state methods rather than direct measurements of vapor bubbles overestimate entrapment depths. Overall, we show that direct measurements of melts and vapor bubbles by SIMS and Raman Spectroscopy, combined with a suitable H_2O - CO_2 solubility model, is a powerful tool to identify the magma storage reservoirs supplying volcanic eruptions.

Plain Language Summary

Pockets of frozen magma trapped within olivine crystals, termed “melt inclusions”, can provide information about the depths at which magma is stored beneath the surface prior to a volcanic eruption. This is because the amount of CO_2 and H_2O that can be dissolved in a melt is dependent on the pressure, and therefore the depth. We examine melt inclusions from lava flows produced during the 2018 eruption of Kīlauea Volcano. Previous geophysical work has shown that magma is stored in two main reservoirs at Kīlauea, located at ~ 1 – 2 km and ~ 3 – 5 km depth.

58 However, because many melt inclusions host almost all of their CO₂ within a vapor
59 bubble, which is rarely measured, previous petrological estimates of magma storage
60 depths at Kīlauea do not align with the depths of these reservoirs identified by geo-
61 physics. In this study, we measure the amount of CO₂ in the glass and the bubble
62 using Secondary Ion Mass Spectrometry (SIMS) and Raman Spectroscopy respec-
63 tively. By adding these two measurements together, we can reconstruct the amount
64 of CO₂ that was present when melt inclusions were trapped. Calculated depths align
65 remarkably well with geophysical estimates, and demonstrate that the 2018 eruption
66 was supplied by both magma storage reservoirs.

67 1 Introduction

68 The 2018 lower East Rift Zone (LERZ) eruption was the largest and most
69 destructive in the last 200 years of activity at Kīlauea Volcano, Hawai'i (Neal et
70 al., 2019), accompanied by the highest co-eruptive fluxes of SO₂ ever measured at
71 Kīlauea (up to 200 kt a day; Kern et al., 2020; Whitty et al., 2020), and very high
72 lava effusion rates (100-300 m³/s; Neal et al., 2019; Patrick, Orr, et al., 2019). Be-
73 fore the onset of this new eruptive episode in May 2018, Kīlauea had been erupting
74 near-continuously for 35 years on the middle East Rift Zone (ERZ) at Pu'u Ō'ō
75 cone and surrounding vents, located approximately ~20 km east of Kīlauea's summit
76 (1983–2018), and ~24 km uprift of the 2018 eruption site (Fig. 1b). From 2008 to
77 2018, a persistently active lava lake was also present within Halema'uma'u (HMM)
78 pit crater, located in the south west area of Kīlauea's summit caldera (Fig. 1b).

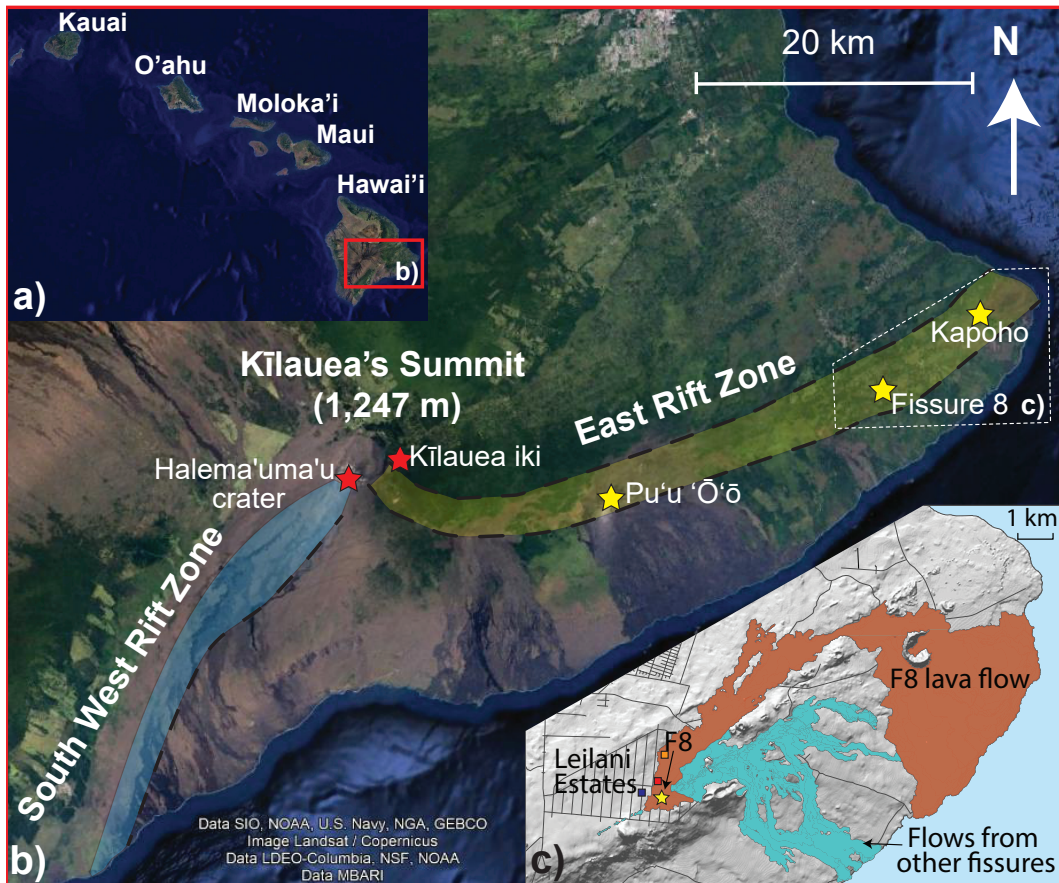


Figure 1. Map of Kīlauea Volcano (b), located on the southwest of the island of Hawai'i (a). Two prominent rift zones radiate from Kīlauea's summit caldera (b). The 2018 eruption occurred within the Leilani Estates subdivision on the lower East Rift Zone (LERZ; expanded region in c). The lava flows from Fissure 8 (marked with a yellow star) are colored deep orange, while flows from Fissures 1–7, and 9–24 are colored light blue. Sample locations are marked with squares (blue=May, 2018, red=July, 2018, orange=Aug, 2018). Base maps for a) and b) are from Google Earth, and the map in c) is adapted from Patrick, Orr, et al. (2019).

79 The 2018 eruption was preceded by swarms of lower-crustal earthquakes at
 80 ~6–12 km depth beneath Kīlauea's summit area on March 7th, April 11th, and
 81 April 18th, 2018 (Flinders et al., 2020). This inflation has been variably interpreted
 82 to result from a short-term increase in magma supply (Flinders et al., 2020), or a
 83 decrease in the output of magma along the ERZ to Pu'u 'Ō'ō, leading to magma
 84 backing up within the summit reservoir (Patrick et al., 2020). On March 13th,
 85 2018, inflation was recorded by tiltmeters located at Kīlauea's summit. Inflationary

86 ground deformation also began at Pu‘u ‘Ō‘ō, suggesting that excess magma was
87 accumulating beneath this vent (Neal et al., 2019). The pressurization at these two
88 locations continued throughout March and April, demonstrated by the rise of the
89 lava pond at Pu‘u ‘Ō‘ō, and overflows of the summit lava lake in mid-late April. On
90 April 30th, the crater floor at Pu‘u ‘Ō‘ō collapsed, followed by an eastward migra-
91 tion of seismicity along the rift zone, consistent with the propagation of a dyke (Neal
92 et al., 2019). A hazard notice released early in the morning of May 1st warned the
93 residents of Lower Puna to be alert, as a large area along the ERZ east of Pu‘u ‘Ō‘ō
94 was at risk from a new outbreak of lava. Following the appearance of ground cracks
95 in the Leilani Estates subdivision (Fig. 1c) on May 2nd, lava reached the surface
96 just before 5 pm on May 3rd (Neal et al., 2019). Over the next few days, multiple
97 fissures opened, preceded by gas emissions and ground cracking. In all, 24 fissures
98 opened between the 3rd and 27th of May 2018.

99 Activity between the 3rd and 9th of May, classified as Early Phase 1 by
100 Gansecki et al. (2019), was characterized by the eruption of spatter mounds and
101 sluggish, slow-moving lava flows. This relatively evolved magma (mean $\text{SiO}_2=51$
102 wt% and $\text{MgO}=4$ wt%; Lee et al., 2019; Gansecki et al., 2019) is thought to have
103 formed by differentiation within LERZ storage reservoirs over decades to centuries
104 (Neal et al., 2019). Throughout May, the compositions of erupted melts and crys-
105 tals became increasingly primitive as summit-derived magma flushed out the LERZ
106 storage reservoirs, with the exception of the involvement of an andesitic composition
107 erupted in mid to late May (Gansecki et al., 2019). The eruption of hotter, less vis-
108 cous lava led to the generation of fast-moving lava flows on May 18th, which reached
109 the coast five days later (Neal et al., 2019, Fig. 1c). By May 28th, activity had lo-
110 calized at Fissure 8 (F8), with the effusion of fast-flowing magma as a channelized
111 flow (Patrick, Dietterich, et al., 2019). Activity ended abruptly on August 4th, by
112 which time F8 had erupted $\sim 1.5 \text{ km}^3$ of lava (Kauahikaua & Trusdell, 2020).

113 Despite the abundant geophysical and geochemical observations made during
114 the LERZ eruption, the source of the magma erupted at F8 from late May-August
115 2018 has not yet been established. It is generally accepted that two main reservoirs
116 are located beneath Kilauea’s summit. The shallower Halema’uma’u (HMM) reser-
117 voir is recognised as an inflation source located beneath the eastern rim of the HMM
118 crater, and is thought to be centred at $\sim 0.5\text{--}2$ km depth (Anderson et al., 2019;

119 Cervelli & Miklius, 2003; Baker & Amelung, 2012; Fiske & Kinoshita, 1969), while
120 the deeper South Caldera (SC) reservoir manifests as an inflation source located
121 beneath the southern portion of the caldera, at $\sim 3\text{--}5$ km depth (Baker & Amelung,
122 2012; Poland et al., 2015). The 2018 LERZ eruption was accompanied by large-scale
123 subsidence of the caldera floor centred around the HMM crater (500 m in certain
124 locations; Neal et al., 2019), which has been attributed to magma withdrawal from
125 the underlying HMM reservoir to feed the effusion of lava from F8 (Anderson et al.,
126 2019). However, recent estimates of the total SO_2 emissions requires the erupted vol-
127 ume to be approximately twice the modelled volume loss from the HMM reservoir,
128 suggesting that a second magma source was involved (Kern et al., 2020).

129 Additionally, the erupted crystal cargo from F8 contained some of the most
130 forsteritic olivines ($\text{Fo}_{88\text{--}89}$) erupted at Kīlauea since 1974, which must have grown
131 in melts with 13–14 wt% MgO (Gansecki et al., 2019). Some of these crystals also
132 contain prominent kink bands (Gansecki et al., 2019), indicating that their crystal
133 lattices have been deformed (Wieser, Edmonds, et al., 2020). Previous work has
134 suggested that highly forsteritic, deformed olivines are derived from the deeper,
135 SC reservoir at 3–5 km depth (Helz et al., 2014, 2015; Wieser et al., 2019; Wieser,
136 Edmonds, et al., 2020), or Kīlauea’s deep rift zones at 6–9 km depth (Clague & Den-
137 linger, 1994; Vinet & Higgins, 2010). Alternatively, Lynn et al. (2017) suggest that
138 highly forsteritic olivines from the Keanakāko’i Tephra may originate from deeper
139 crustal storage reservoirs, perhaps located near the base of the volcanic pile at $\sim 8\text{--}10$
140 km depth.

141 Our study utilizes the strong pressure dependence of the solubility of CO_2 (and
142 H_2O) in silicate melts to determine the pressures at which pockets of melt, termed
143 melt inclusions, were trapped within olivine crystals. Through prior constraints
144 on the density profile of the crust, entrapment pressures from F8 melt inclusions
145 erupted in late May, mid-July and early August 2018 can be converted into entrap-
146 ment depths. In turn, these depths can be compared to geophysical estimates of the
147 depths of the main magma storage regions at Kīlauea to determine the source(s) of
148 magma erupted at F8.

2 Melt Inclusion Entrapment Pressures

2.1 The Importance of Vapor Bubbles

The solubility of pure CO₂ and H₂O in silicate melts is dependent on the pressure, the major element content of the melt, and the melt temperature. Assuming that a melt was saturated in a CO₂-H₂O fluid phase at the time of melt inclusion formation, the pressure at which a melt inclusion was trapped can be calculated by reconstructing its initial volatile and major element composition. In relatively water-poor systems like Kilauea, where melts contain <1 wt% H₂O (Dixon et al., 1991; Clague et al., 1995; Sides, Edmonds, Maclennan, Swanson, & Houghton, 2014; Sides, Edmonds, Maclennan, Houghton, et al., 2014; Tucker et al., 2019; Wallace & Anderson, 1998), the entrapment pressure is most sensitive to the CO₂ content of the melt, and its major element composition. Variations in melt H₂O content between 0–1 wt% have a relatively small effect on the entrapment pressure (except at very low CO₂ contents; see Supporting Information Fig. S1; Newman & Lowenstern, 2002).

However, estimating the CO₂ content of a melt inclusion at the point of entrapment is not straightforward. The host crystal may experience a period of cooling after the melt inclusion was trapped, leading to the growth of olivine on the walls of the inclusion (termed post-entrapment crystallization, or PEC; Roedder, 1984; Danyushevsky et al., 2000; Anderson & Brown, 1993). The precipitation of denser olivine from the silicate melt, combined with the differential thermal contraction of the melt phase and the host olivine, causes the internal pressure of the melt inclusion to drop, driving the growth of a vapor bubble (Roedder, 1979; Anderson, 1974; Anderson & Brown, 1993). Combined with a reduction in the solubility of CO₂ associated with major element changes during PEC, these processes cause CO₂ to migrate from the melt phase into the bubble (Steele-Macinnis et al., 2011; Sides, Edmonds, Maclennan, Houghton, et al., 2014; Maclennan, 2017; Aster et al., 2016). An additional phase of bubble growth is caused by the differential thermal contraction of the melt inclusion and the host olivine during syn-eruptive cooling from high magmatic temperatures (~1150° C at F8; Helz & Thornber, 1987; Gansecki et al., 2019) to the glass transition temperature (~725°C; Ryan & Sammis, 1981).

180 Unfortunately, the vast majority of published volatile contents in melt in-
181 clusions globally, and at Kilauea, only measured CO₂ in the glass phase, using
182 techniques such as secondary-ion mass spectrometry (SIMS), or Fourier transform
183 infrared spectroscopy (FTIR; Bennett et al., 2019; Ruth et al., 2018; Sides, Ed-
184 monds, Maclennan, Houghton, et al., 2014; Sides, Edmonds, Maclennan, Swanson,
185 & Houghton, 2014). Given that recent work has shown that ~40–90% of the total
186 CO₂ budget of melt inclusions may be held within the vapor bubble (Hartley et al.,
187 2014; Wallace et al., 2015; Moore et al., 2015; Rasmussen et al., 2020), entrapment
188 pressures from studies neglecting vapor bubble carbon must be viewed as minimum
189 estimates (Anderson & Brown, 1993; Ruth et al., 2018).

190 **2.2 Reconstructing Vapor Bubble CO₂**

191 Several approaches have been used to explore the contribution of vapor bubbles
192 to the CO₂ budget of Hawaiian melt inclusions. Anderson and Brown (1993) theo-
193 retically reconstruct vapor bubble CO₂ by assuming that the melt and vapor bubble
194 were in chemical equilibrium at high magmatic temperatures prior to syn-eruptive
195 quenching. Specifically, they calculated melt inclusion internal pressures from glass
196 CO₂ contents, and used these pressures to determine the molar volume of CO₂ in
197 vapor bubbles using the CO₂ equation of state (EOS). They converted their molar
198 volumes into CO₂ concentrations assuming that bubbles occupied 0.5 vol% of the
199 melt inclusion prior to quenching, and added these values to measurements of glass
200 CO₂ concentrations. Riker (2005) used a similar method to reconstruct bubble car-
201 bon for melt inclusions from the 1859 eruption of Mauna Loa. However, instead of
202 using a fixed bubble volume, they account for the differential amounts of cooling
203 and PEC experienced by erupted crystals, and calculate the bubble volumes prior to
204 quench-induced expansion as a function of the drop in temperature (ΔT) between
205 the melt inclusion at the point of entrapment and eruption ($\text{VB vol\%} = 0.0162 \Delta T$
206 $- 0.0016$). More recently, Tucker et al. (2019) theoretically reconstructed bubble
207 carbon contents for a large suite of melt inclusions from several Hawaiian volcanoes,
208 including 167 from Kilauea. However, instead of estimating the size of the vapor
209 bubble prior to syn-eruptive quenching as in Anderson and Brown (1993) and Riker
210 (2005), they used observed bubble volumes to convert CO₂ densities obtained from
211 the EOS into bubble CO₂ concentrations. This approach is problematic because ex-

212 pansion of the bubble during syn-eruptive cooling and quenching continues until the
213 glass transition temperature, while CO₂ diffusion through the melt into the bubble
214 may effectively cease at a higher temperature. Thus, the final stages of bubble ex-
215 pansion will occur without concurrent CO₂ diffusion from the glass into the bubble,
216 meaning that the EOS method will overpredict the amount of CO₂ in the bubble
217 (Anderson & Brown, 1993; Maclennan, 2017; Rasmussen et al., 2020).

218 The total amount of CO₂ within melt inclusions can also be determined using
219 experimental homogenization techniques, where crystals containing melt inclusions
220 are heated to magmatic temperatures. This drives the dissolution of the olivine
221 rim precipitated during PEC, which changes the chemistry and volume of the melt
222 inclusion so that CO₂ held within the vapor bubble dissolves back into the melt.
223 Following rapid quenching, the glass phase of these rehomogenized melt inclusions
224 can be analyzed by SIMS or FTIR (Esposito et al., 2012; Rasmussen et al., 2020;
225 Skirius et al., 1990; Tuohy et al., 2016; Wallace et al., 2015). However, experimental
226 homogenization can lead to H₂O loss, excess dissolution of olivine on the walls of
227 the melt inclusion, and loss of mineral and melt inclusion zoning, which degrades
228 the overall utility of the melt inclusion record (Rasmussen et al., 2020; Tuohy et al.,
229 2016). Additionally, it is not always possible to fully dissolve the original bubbles,
230 and new bubbles containing CO₂ may nucleate upon quench (Wallace et al., 2015;
231 Tuohy et al., 2016; Skirius et al., 1990; Rasmussen et al., 2020).

232 Most recently, the density of CO₂ in vapor bubbles has been measured di-
233 rectly using Raman Spectroscopy (Esposito et al., 2011; Steele-Macinnis et al.,
234 2011; Hartley et al., 2014; Moore et al., 2015, 2018; Aster et al., 2016; Taracsák et
235 al., 2019). The Raman spectrum of CO₂ consists of two peaks nominally at 1285
236 cm⁻¹ and 1388 cm⁻¹ at 1 bar (see Supporting Information Fig. S2), resulting from
237 the interaction of a symmetrical stretching mode and an active bending mode in
238 the CO₂ molecule by a process known as Fermi resonance (Rosso & Bodnar, 1995;
239 Lamadrid et al., 2017; Fermi, 1931). Hence, collectively, these peaks are referred to
240 as the Fermi diad (FD), and the distance between the peak centres is the Fermi diad
241 splitting (Δ). However, while it is well accepted that Δ correlates with CO₂ den-
242 sity (ρ_{CO_2}), there are a number of different parameterizations for this relationship
243 in the literature (Wang et al., 2019; Rosso & Bodnar, 1995; Lamadrid et al., 2017;
244 Kawakami et al., 2003, and refs. within). The diversity of published densimeters

245 reflects different instrument hardware, as well as the choice of analytical conditions
 246 (Lamadrid et al., 2017). Thus, the approach used by a number of studies where a
 247 densimeter is chosen from the literature to convert measurements of Δ to ρ_{CO_2} on a
 248 different Raman instrument from the one used to calibrate the densimeter results in
 249 large systematic uncertainties in the absolute density of CO_2 (e.g., Venugopal et al.,
 250 2020; Taracsák et al., 2019; Hartley et al., 2014). For example, $\Delta=102.8 \text{ cm}^{-1}$ yields
 251 $\rho_{CO_2}=0.0281 \text{ g/cm}^3$ using the densimeter of Wang et al. (2019), but $\rho_{CO_2}=0.1397$
 252 g/cm^3 using the densimeter of Kawakami et al. (2003). For a bubble volume of 5%
 253 (the 80th percentile of bubble volume proportions at Kilauea from Tucker et al.,
 254 2019) and a melt density of 2.75 g/cm^3 , these different densimeters predict a con-
 255 tribution of 538 ppm vs. ~ 2674 ppm CO_2 to the reconstructed total CO_2 budget
 256 of the melt inclusion. For a melt inclusion with $SiO_2=49 \text{ wt\%}$, and $H_2O=0.5 \text{ wt\%}$,
 257 these CO_2 contents correspond to entrapment pressures of $\sim 1.2 \text{ kbar}$ vs. 4.8 kbar
 258 (at 1200°C ; Newman & Lowenstern, 2002), and entrapment depths of $\sim 4 \text{ km}$ vs.
 259 $\sim 18 \text{ km}$ respectively for a crustal density of 2700 kg/m^3 . This demonstrates that
 260 the development of an instrument-specific calibration is essential to be able to dif-
 261 ferentiate between lower and upper crustal storage at ocean island volcanoes, let
 262 alone fingerprinting the involvement of different reservoirs identified by geophysical
 263 techniques.

264 An additional source of error affecting both Raman measurements and EOS
 265 methods arises during the conversion of ρ_{CO_2} into the equivalent amount of CO_2 in
 266 ppm held within the vapor bubble ($[CO_2]^{VB}$):

$$[CO_2]^{VB} = 10^6 \times \frac{\rho_{CO_2} V_{VB}}{\rho_{Melt} V_{Melt}} \quad (1)$$

267 Where V_{VB} and V_{Melt} are the volume of the vapor bubble and the melt phase of
 268 the inclusion respectively, and ρ_{Melt} is the density of the silicate melt calculated
 269 here using DensityX (Iacovino & Till, 2019). Total CO_2 contents are obtained by
 270 summing the equivalent amount of CO_2 in the vapor bubble with the concentration
 271 of CO_2 measured in the melt phase ($[CO_2]^{Melt}$) by SIMS or FTIR:

$$[CO_2]^{Tot} = [CO_2]^{VB} + [CO_2]^{Melt} \quad (2)$$

272 The volumes of the vapor bubble and melt inclusion are typically determined
 273 from 2D transmitted light images, estimating the length of the third, unmeasurable

274 dimension from the major and minor axes of the plan view of the inclusion. Tucker
 275 et al. (2019) simulate this process by randomly intersecting ellipses and show that
 276 the smallest errors are achieved by calculating the third dimension as the arithmetic
 277 mean of the two measured axes. However, this approach is still associated with a 1σ
 278 error of -47 to +37% (Tucker et al., 2019). Although important, we note that this
 279 random error is entirely overwhelmed by the systematic error of up to a factor of 4
 280 in literature datasets which have arbitrarily chosen a literature densimeter.

281 To mitigate the systematic error associated with Raman calibration, we de-
 282 termine the relationship between Δ and ρ_{CO_2} for the specific instrument and ac-
 283 quisition conditions used in this study through the analysis of synthetic fluid melt
 284 inclusions with known CO_2 densities. Analysis of both the melt phase (using SIMS)
 285 and the vapor bubble (using a calibrated Raman system) yields the first extensive
 286 dataset critically evaluating the contribution of vapor bubbles to the total CO_2 bud-
 287 get of specific melt inclusions at Kīlauea. Combined with a rigorous examination of
 288 the suitability of different CO_2 - H_2O solubility models, these measurements place
 289 accurate constraints on entrapment depths of olivine-hosted melt inclusions from the
 290 2018 LERZ eruption. This dataset, combined with quantitative models of bubble
 291 growth, also allows assessment of the relative importance of post-entrapment crys-
 292 tallization and syn-eruptive quenching on the partitioning of CO_2 between the melt
 293 and vapor phase. In turn, this allows the accuracy of EOS methods as an alternative
 294 to direct measurements of ρ_{CO_2} using Raman Spectroscopy to be evaluated.

295 **3 Materials and Methods**

296 **3.1 Sample Details, Preparation and Analytical Methods**

297 We examine three samples erupted at F8 (square symbols; Fig. 1c):

- 298 1. May-18 (erupted May 30th, 2018; USGS code KE62-3293; blue symbols),
 299 comprising vesicular reticulite and scoria which landed in a bucket placed near
 300 the F8 vent ($19^\circ 27.7486'$ N, $154^\circ 54.8636'$ W).
- 301 2. July-18 (erupted Mid-July 2018; red symbols), from the selvages of a
 302 naturally-quenched, and highly vesicular proximal overflow from the F8 chan-
 303 nel (<50 m from the vent; $19^\circ 27.879'$ N, $154^\circ 54.645'$ W).

304 3. Aug-18 (erupted Aug 1st; USGS code KE62-3321F; orange symbols), which
305 was sampled directly from the F8 channel using a metal rod and chain, and
306 rapidly quenched in water. Direct lava sampling took place on a stable chan-
307 nel levee ($19^{\circ} 28.31508' \text{ N}$, $154^{\circ} 54.51426' \text{ W}$), $\sim 700 \text{ m}$ downstream of the
308 position of the July-18 overflow.

309 Samples were jaw crushed and sieved into three size fractions (250–840, 840–
310 1000 and $>1000 \mu\text{m}$). Olivines were picked under a binocular microscope, and in-
311 dividually mounted in CrystalBondTM on glass slides. Care was taken to prepare
312 melt inclusions hosted within olivine crystals from all three size fractions. Melt in-
313 clusions were exposed by grinding with 250–3000 grade wet and dry paper, allowing
314 embayments to be avoided, and melt inclusions containing vapor bubbles to be iden-
315 tified. Melt inclusions without vapor bubbles were ground down with progressively
316 finer wet and dry paper until the center of the inclusion was exposed. Melt inclu-
317 sions containing vapor bubbles were ground down to just above the top of the melt
318 inclusion of interest (to avoid intersecting the bubble, and releasing the trapped
319 CO_2). A photo was taken of the melt inclusion and vapor bubble using a transmit-
320 ted light microscope to allow estimation of melt inclusion and bubble volumes. For
321 larger melt inclusions, two images were acquired: one where the bubble was in focus,
322 and one where the melt inclusion outline was in focus. The outline of the bubble
323 and melt inclusion were traced using ImageJ (Schneider et al., 2012), and a best
324 fit ellipse was fitted to each. Volumes were calculated by assuming that the third
325 (non-measurable dimension) was equal to the arithmetic mean of the two measured
326 dimensions (Tucker et al., 2019). Several melt inclusions contained large spinel crys-
327 tals that were likely co-entrapped. The volume of these spinels (assuming a cuboid
328 shape, with the third dimension also equal to the arithmetic mean of the visible
329 dimensions) was subtracted from the volume of the melt inclusion.

330 Following optical measurements, crystals were ground down until the vapor
331 bubble was within $\sim 30 \mu\text{m}$ of the surface. Depending on the optical quality after
332 fine grinding (using 2000-7000 grade wet and dry paper), melt inclusions were vari-
333 ably polished using $9 \mu\text{m}$ diamond pastes prior to Raman analysis. Raman spectra
334 of vapor bubbles were collected using a confocal LabRAM 300 (Horiba Jobin Yvon)
335 Raman spectrometer in the Department of Earth Sciences at the University of Cam-

336 bridge. The two CO₂ Fermi Diads were fitted with Gaussians (see Supporting Infor-
 337 mation Fig. S4). The relationship between the Δ and ρ_{CO_2} for the specific Raman
 338 acquisition condition used in this study was determined by analyzing 16 synthetic
 339 CO₂ – H₂O fluid melt inclusions with a range of densities (~ 0.04 g/cm³, ~ 0.08
 340 g/cm³ and ~ 0.14 g/cm³) hosted in quartz, as well as three Kīlauean melt inclusion
 341 vapor bubbles. The densities of all 19 of these primary standards were measured
 342 using a JY Horiba LabRam HR in the Fluids Research Laboratory at Virginia Tech
 343 Raman, which has been specifically calibrated for low CO₂ densities using a high-
 344 pressure optical cell (Lamadrid et al., 2017). A linear regression through repeated
 345 measurements of standards yielded the following relationship with 95% confidence
 346 intervals on the regression (see Supporting Information Fig. S3):

$$\rho_{CO_2}(\text{g/cm}^3) = 0.3217 \pm 0.026 \Delta (\text{cm}^{-1}) - 32.995 \pm 2.7 \quad (3)$$

347 Further analytical details are presented in the Supporting Information (Text
 348 S1). Following Raman analyses, individual crystals were ground down to expose the
 349 center of each melt inclusion to maximize the available analyzable area. The bubble
 350 was exposed in approximately half of bubble-bearing inclusions. Following sonication
 351 to remove polishing residue, exposed bubble walls were examined on the FEI Quanta
 352 650FEG SEM at the University of Cambridge in low vacuum mode prior to the ap-
 353 plication of any coatings. Crystals were then mounted in epoxy in groups of 20–40,
 354 and polished with progressively finer diamond pastes (9, 6, 3, 1, 0.25 μm).

355 Following the application of a gold coat, the concentrations of H₂O and CO₂
 356 (as well as MgO and SiO₂ for normalization) in melt inclusions and co-erupted
 357 matrix glasses were determined using the Cameca IMS-7f GEO at the NERC Ion
 358 Microprobe Facility, University of Edinburgh. SIMS analysis was performed prior to
 359 EPMA analysis to avoid volatile migration under the electron beam, and to avoid
 360 contamination of measured carbon concentrations by a carbon coat. Epoxy stubs
 361 were placed in the sample chamber at vacuum for a minimum of 6 hours before
 362 analysis to allow them to outgas. A wide variety of standards were analyzed to cre-
 363 ate calibration curves for H₂O and CO₂ (N71, M10, 519-4-1, M5, M40, M36, M21,
 364 M47, M36; see Supporting Information S5; Shishkina et al., 2010; Hauri, 2002).
 365 Additional information regarding calibration, background and drift corrections are
 366 provided in the Supporting Information (Text S2).

367 Following SIMS analyses, the Au coat was removed by polishing on a 0.25 μm
 368 diamond polishing pad, and a carbon coat was applied for electron microprobe an-
 369 alyzer (EPMA) analyses. Spot analyses of melt inclusions, matrix glasses and host
 370 olivines were obtained using a Cameca SX100 EPMA in the Department of Earth
 371 Sciences, University of Cambridge following the two-condition analytical set up de-
 372 scribed in Wieser et al. (2019). Spectrometer configurations, count times, calibration
 373 materials, and estimates of precision and accuracy calculated from repeated analyses
 374 of secondary standards (San Carlos Olivine, VG2 and A99; Jarosewich, 2002) are
 375 presented in the Supporting Information (Text S3, Tables S2-4).

376 Melt inclusions were corrected for the effects of post-entrapment crystalliza-
 377 tion using the Olivine MI tool in Petrolog3 (Danyushevsky & Plechov, 2011). This
 378 requires the user to specify the initial FeO_T and the host Fo content of each inclu-
 379 sion. FeO_T was set at 11.33 wt% for melt inclusions hosted in olivines with forsterite
 380 contents ($[\text{Fo}=\text{Mg}^{2+}/(\text{Mg}^{2+}+\text{Fe}^{2+}) \text{ atomic}]>79 \text{ mol\%}$ based on the liquid line of
 381 descent at Kilauea, and for consistency with previous studies (Wieser et al., 2019;
 382 Sides, Edmonds, Maclennan, Swanson, & Houghton, 2014). For olivine crystals with
 383 $\text{Fo}<79 \text{ mol\%}$, the initial FeO content was estimated from the relationship between
 384 the equilibrium olivine forsterite content and melt FeO_T contents in a fractional
 385 crystallization model computed in MELTS for MATLAB (Supporting Information
 386 Fig. S5 Antoshechkina & Ghiorso, 2018).

387 4 Results

388 F8 melt inclusions are hosted in olivine crystals with a wide range of core com-
 389 positions (Fo_{77-89} ; Fig. 2a). Core compositions in all three samples show a peak
 390 at $\sim\text{Fo}_{88-89}$ (Fig. 2b-d), which lies significantly above the equilibrium field cal-
 391 culated from the Mg# of co-erupted matrix glasses [$\text{Mg\#}=\text{Mg}^{2+}/(\text{Mg}^{2+}+\text{Fe}^{2+})$,
 392 atomic], even considering a wide range of experimentally-determined values for
 393 $K_{D_{\text{Fe}^{2+}}^{\text{ol-melt}}}$ (black lines, Fig. 2a; 0.270–0.352; Roeder & Emslie, 1970; Matzen et
 394 al., 2011). Fourteen melt inclusions from May-18, but only six melt inclusions from
 395 July-18 and one from Aug-18 are hosted in olivines which lie within the equilibrium
 396 field. F8 olivines have some of the highest Fo contents ever reported at Kilauea (Fig.
 397 2a-d vs. Fig. 2e-f; Sides, Edmonds, Maclennan, Swanson, & Houghton, 2014; Wieser
 398 et al., 2019), but relatively low carrier melt Mg#s (51–57 mol%; assuming $\text{Fe}^{3+}/\text{Fe}_T$

399 = 0.15). In turn, this juxtaposition produces some of the most extreme degrees of
400 olivine-carrier melt Fe-Mg disequilibrium seen at Kīlauea (Fig. 2a). Crystals with
401 high forsterite cores show strong normal zoning, while those with core compositions
402 plotting closer to the equilibrium field on Fig. 2a are not visibly zoned in rapid EDS
403 acquisitions (see Supporting Information Figs. S7-9).

404 The majority of F8 melt inclusions exhibit lower measured FeO_T contents
405 than co-erupted matrix glasses and the composition of Kīlauean melt inclusions
406 from the literature (grey dots; Wieser et al., 2019; Tucker et al., 2019; Sides, Ed-
407 monds, MacLennan, Houghton, et al., 2014; Sides, Edmonds, MacLennan, Swan-
408 son, & Houghton, 2014). Melt inclusion MgO contents are more similar to those of
409 co-erupted matrix glasses (Fig. 3a). Following a correction for the effects of post-
410 entrapment crystallization, F8 melt inclusions have MgO contents between 6.4 and
411 13.7 wt%, and FeO_T contents between 11.3 and 12 wt% (Fig. 3a, Supporting In-
412 formation Fig. S5). Despite the high degree of Mg# disequilibrium between olivine
413 crystals and their carrier melts (Fig. 2a), measured melt inclusion Mg#s (uncor-
414 rected for the effects of PEC) mostly lie within, or close to the equilibrium field
415 calculated from the core compositions of their host olivines (Fig. 3b). The distance
416 from the equilibrium field degree is largest in the July-18 sample, but still smaller
417 than the vast majority of melt inclusions data from other Kīlauean eruptions, par-
418 ticularly those hosted in olivines with higher Fo contents (Fig. 3b). Melt inclusions
419 hosted in olivine crystals which have the highest degree of disequilibrium with their
420 carrier melts (calculated by subtracting the equilibrium Fo content of the co-erupted
421 matrix glass from the Fo content of each olivine) have experienced the most PEC
422 (Fig. 3c) and have the lowest measured FeO_T contents (Fig. 3d).

423 To encapsulate the variable degrees of olivine-melt disequilibrium, and to aid
424 comparisons between different crystal populations, we subdivide F8 olivines into two
425 groups. The first group contains olivines which lie within, or close to the equilib-
426 rium field calculated from the Mg# of the co-erupted matrix glass (Fig. 2a). For
427 the May-18 sample, the division was placed at $\text{Fo}_{81.5}$, based on the near continuous
428 distribution of olivines from slightly above to within the equilibrium field (which can
429 easily be generated by slight cooling between crystallization and eruption), and the
430 slight gap between these olivines and those with higher Fo contents (Fig 2b). The
431 second group contains olivines which lie outside the equilibrium field. For brevity,

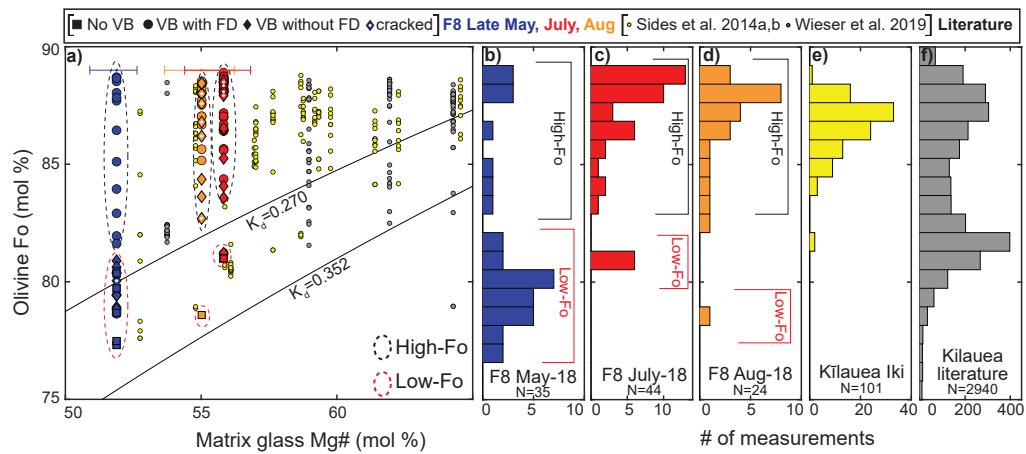


Figure 2. Olivine populations and olivine-melt relationships at F8 compared to literature data. a) Core olivine forsterite content versus matrix glass Mg# for $\text{Fe}^{3+}/\text{Fe}_T=0.15$ (Moussallam et al., 2016; Helz et al., 2017). Olivines lying between the black lines ($K_D=0.270-0.352$) are in equilibrium with their carrier melts considering the range of experimentally-determined Fe-Mg partition coefficients (Roeder & Emslie, 1970; Matzen et al., 2011). F8 olivines have some of the highest Fo contents observed at Kilauea, yet are hosted in carrier liquids with some of the lowest Mg#s. Literature data from Wieser et al. (2019), Sides, Edmonds, Maclennan, Houghton, et al. (2014), Sides, Edmonds, Maclennan, Swanson, and Houghton (2014). b-d) Histograms of olivine Fo contents from this study, e) Kilauea Iki (Sides, Edmonds, Maclennan, Houghton, et al., 2014; Sides, Edmonds, Maclennan, Swanson, & Houghton, 2014), and f) the compilation of literature analyses presented in Wieser et al. (2019) combined with new measurements from Tucker et al. (2019). The strong bimodality in F8 forsterite contents, along with the degree of olivine-melt disequilibrium was used to subdivide melt inclusions into those hosted within High-Fo olivines (black dotted outline) and Low-Fo olivines (red dotted outline). Olivines are further subdivided into those hosting a melt inclusion without a vapor bubble (no VB), with a vapor bubble which produces a Fermi diad (VB with FD), those with a vapor bubble that does not produce a Fermi diad (VB without FD). Melt inclusions which are cracked, and have a vapor bubble without a FD, are indicated with a white dot.

432 these groups are referred to as Low-Fo and High-Fo olivines, although this classi-
 433 fication evaluates the forsterite content of the olivine relative to the Mg# of the
 434 co-erupted matrix glass, rather than the absolute Fo content (see Fig. 3c). A sim-

435 ilar classification for the eruptions on Fig. 2 with higher glass Mg#s would place
436 the boundary between groups at higher Fo contents (e.g., the Fo₈₄ division used by
437 Wieser et al., 2019).

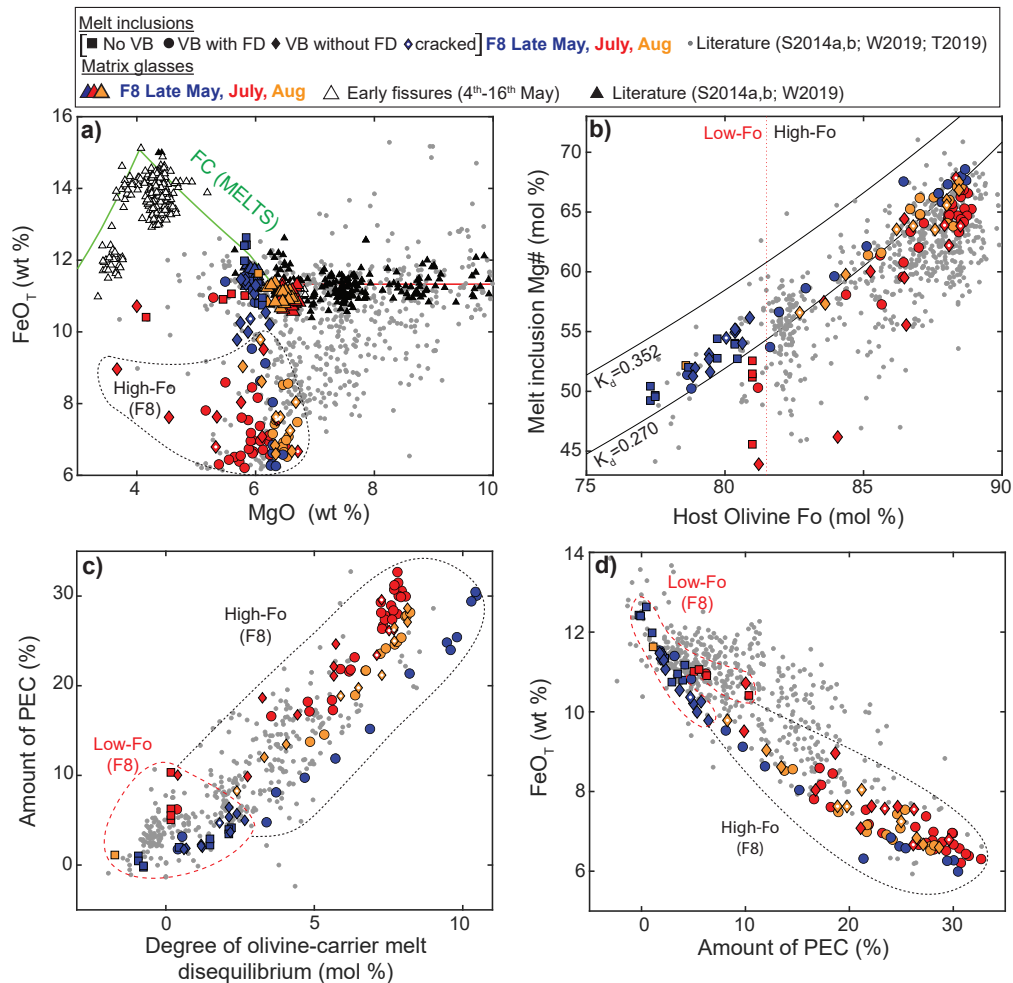


Figure 3. Measured major element systematics for F8 melt inclusions (uncorrected for the effects of PEC). a) High-Fo F8 melt inclusions have significantly lower FeO_T contents than liquid line of descent defined by Kilauean matrix glasses from (this study, Wieser et al., 2019; Sides, Edmonds, MacLennan, Houghton, et al., 2014), and a MELTS for MATLAB (Antoshechkina & Ghiorso, 2018) fractionation path following the onset of clinopyroxene and plagioclase fractionation (green line) which recreates glass compositions erupted from earlier, more evolved fissures during the 2018 eruption (4-5 wt% MgO, white triangles). Despite highly variable FeO_T contents, the MgO contents of melt inclusions mostly align with those of their co-erupted matrix glasses. b) In contrast to the prominent disequilibrium between High-Fo olivine compositions and co-erupted matrix glasses (Fig. 1a), melt inclusion Mg#s uncorrected for the effects of PEC (for $\text{Fe}^{3+}/\text{Fe}_T=0.15$) plot close to the equilibrium field with their host olivines (particularly melt inclusions from the May-18 and Aug-18 samples). Melt inclusions from previous Kilauean eruptions (Wieser et al., 2019; Tucker et al., 2019; Sides, Edmonds, MacLennan, Houghton, et al., 2014; Sides, Edmonds, MacLennan, Swanson, & Houghton, 2014, grey dots) lie much further below the equilibrium field. c) The amount of PEC (calculated in Petrolog3; Danyushevsky & Plechov, 2011) is strongly correlated with the degree of ol-melt disequilibrium, calculated by subtracting the equilibrium olivine composition of the co-erupted matrix glass (for $K_D=0.3$) from the measured Fo content. d) The FeO_T contents of F8 melt inclusions also shows a strong negative correlation with the amount of PEC, extending to lower values than the vast majority of

438 All High-Fo melt inclusions contain a vapor bubble (Fig. 3c), 73% (N=53) of
439 which produce a Fermi diad (FD) during Raman analysis. Vapor bubbles which do
440 not produce a FD may contain no CO₂, or CO₂ densities below the detection limit
441 of Raman spectroscopy. While the detection limit will depend on the exact depth
442 of the bubble below the surface, as well as the transparency of the host crystal, the
443 distribution of densities in vapor bubbles which produced a FD indicates that the
444 detection limit lies between 0–0.02 g/cm³ (light green bar in Fig. 4c). Nine of the
445 bubbles without a FD are hosted within cracked melt inclusions, which may have
446 resulted in CO₂ loss from the bubble (diamonds with white dots; Fig. 3 and 4, see
447 Supporting Information Fig. S10 Aster et al., 2016). In contrast, only 50% (N=15)
448 of Low-Fo melt inclusions contain a vapor bubble, and only 20% (N=3) of these pro-
449 duce a FD (Fig. 3c). Only 1 of the bubbles without a FD is hosted within a cracked
450 melt inclusion.

451 Bubble-bearing melt inclusions show a correlation between the volume % of
452 the bubble and the amount of PEC, despite the large random errors associated with
453 measuring bubble proportions from 2D images (grey error bars; Fig. 4a). There is
454 a substantial drop in glass CO₂ contents with increasing PEC, and melt inclusions
455 containing vapor bubbles with a FD show significantly lower glass CO₂ contents
456 than bubble-free melt inclusions (Fig. 4b, $p=10^{-7}$; Kolmogorov Smirnov test).
457 There is no obvious correlation between the CO₂ density in vapor bubbles and the
458 amount of PEC (Fig. 4c, $R^2=10^{-5}$), the CO₂ density and the glass CO₂ content
459 ($R^2=0.1$) or the CO₂ density and the volume of the bubble ($R^2=0.0004$). The me-
460 dian and mean proportion of the total melt inclusion CO₂ budget hosted within the
461 bubble is 93% and 87% respectively (black histogram; Fig. 4d). This exceeds the
462 proportions calculated by Moore et al. (2015) for melt inclusions from the 1959 and
463 1960 eruptions of Kīlauea (median=67%, mean=65%; blue histogram). This dis-
464 crepancy reflects the fact that Moore et al. (2015) did not measure the CO₂ content
465 of the glass in each melt inclusion, so they calculated proportions assuming a glass
466 CO₂ content of 300 ppm (the maximum measured in the same suite of samples by
467 Tuohy et al., 2016). Our new data shows the importance of measuring CO₂ in the
468 glass and bubble of a specific melt inclusion; while bubble-free melt inclusions have
469 CO₂ contents up to 417 ppm in the glass phase, those with vapor bubbles produc-
470 ing a FD have median CO₂ contents of only 45 ppm (mean=54 ppm; Fig. 4b). In

471 contrast to the highly variable CO₂ contents in melt inclusion glasses, H₂O contents
472 are remarkably constant within a given eruption, despite significant variation in the
473 contents of incompatible elements such as Na₂O and K₂O (Fig. 5a). Excluding two
474 degassed melt inclusions (~ 0.09 wt% H₂O), F8 melt inclusions have between 0.19–
475 0.33 wt% H₂O, which is lower than most of the Kīlauean melt inclusions measured
476 by Sides, Edmonds, MacLennan, Houghton, et al. (2014); Sides, Edmonds, MacLen-
477 nan, Swanson, and Houghton (2014) and almost all of those measured by Tucker et
478 al. (2019) (Fig. 5b).

479 5 Discussion

480 5.1 Mineral-melt disequilibrium drives the growth of a CO₂-rich 481 bubble

482 The prominent Mg# disequilibrium between the core compositions of High-Fo
483 olivines from F8 and their carrier melts has been observed in a number of historic
484 eruptions at Kīlauea (Fig. 2; Tuohy et al., 2016; Wieser et al., 2019; Sides, Ed-
485 monds, MacLennan, Houghton, et al., 2014; Sides, Edmonds, MacLennan, Swanson,
486 & Houghton, 2014). Based on major and trace element disequilibrium between melt
487 inclusions and their carrier melts (e.g., Nb/Y ratios), as well as microstructures
488 consistent with deformation of the crystal lattice (also observed in some High-Fo
489 olivines from F8 by Gansecki et al., 2019), Wieser, Edmonds, et al. (2020) and
490 Wieser et al. (2019) suggested that highly forsteritic olivines are scavenged from
491 long-lived plastically-deforming mush piles at the base of the SC reservoir, and
492 incorporated into cooler, lower Mg# carrier melts with different trace element sig-
493 natures just prior to eruption. In contrast, these studies suggest that olivines with
494 lower forsterite contents exhibiting small amounts of olivine-melt disequilibrium
495 (similar to the Low-Fo olivines in this study), no lattice distortions, and a high de-
496 gree of trace element equilibrium may have crystallized from their carrier melts as
497 true phenocrysts.

498 Kīlauean melts with greater than ~ 6.8 wt% MgO are saturated in only olivine
499 and minor chrome-spinel (Wright & Fiske, 1971), so show a strong correlation be-
500 tween temperature and the MgO content of the melt (Helz & Thornber, 1987). The
501 remarkably constant FeO contents of these high MgO melts (Fig. 3a) means that

502 glass Mg# is strongly correlated with MgO, and therefore temperature. As glass
503 Mg# is closely related to the olivine forsterite content through the Fe-Mg olivine-
504 liquid exchange coefficient, equilibrium olivine forsterite contents are also strongly
505 correlated with temperature. Thus, the difference in Mg# between the measured
506 olivine core composition, and the equilibrium olivine forsterite content calculated
507 from the composition of co-erupted matrix glasses (termed the degree of olivine-melt
508 disequilibrium) is proportional to the amount of cooling experienced by the inclu-
509 sion prior to syn-eruptive quenching (Wieser et al., 2019). The close relationship
510 between the amount of cooling experienced by an inclusion, and the amount of PEC
511 (Danyushevsky et al., 2000) accounts for the excellent correlation between the degree
512 of olivine-melt disequilibrium and the amount of PEC (Fig. 3c).

513 F8 melt inclusions are hosted in some of the most forsteritic olivines erupted
514 at Kilauea, yet were erupted in carrier melts with some of the lowest Mg#s (Fig.
515 2a). Consequently, they have experienced some of the largest amounts of cooling
516 following entrapment, and, by extension, some of the largest amounts of PEC ever
517 reported at Kilauea (up to $\sim 33\%$; Fig. 3c). These PEC extents are also signifi-
518 cantly larger than those reported from other volcanic systems; olivine-hosted melt
519 inclusions from Holuhraun (Iceland), Piton de la Fournaise (Réunion) and Erebus
520 (Antarctica) have experienced $\sim 5\%$, $< 12\%$ and $0-4.2\%$ PEC respectively (Hartley
521 et al., 2015; Collins et al., 2012; Moussallam et al., 2014). The small amounts of
522 cooling (and therefore PEC) experienced by Low-Fo olivines, which are close to equi-
523 librium with their carrier melts, likely occurred during fractionation between the
524 formation and eruption of these crystals (Fig. 3c). However, progressive fractiona-
525 tion and cooling of a batch of melt cannot account for the peak at $\sim \text{Fo}_{88-89}$ in F8
526 samples (Wieser et al., 2019; Maaløe et al., 1988), nor the paucity of olivines with Fo
527 contents in equilibrium with the co-erupted matrix glasses (particularly in the July
528 and Aug samples; Fig. 2a). Based on the similarities between the High-Fo olivines
529 from F8 and previous studies (large amounts of olivine-melt disequilibrium, pres-
530 ence of lattice distortions; Gansecki et al., 2019), we appeal to the process proposed
531 by Wieser et al. (2019), where cooling is not a gradual process during progressive
532 differentiation of a given magma batch (Maaløe et al., 1988), but occurs over short
533 timescales, when High-Fo olivine crystals residing in hot mush piles are mixed into

534 significantly cooler, lower Mg# melts (Wieser et al., 2019; Sides, Edmonds, Maclennan,
535 Houghton, et al., 2014), see also Shea et al. (2019).

536 Melt inclusion MgO and FeO_T contents are strongly affected by the crystal-
537 lization of olivine on the walls of the melt inclusion (PEC), and subsequent diffusive
538 re-equilibration. Based on the strong coupling between MgO content and tempera-
539 ture in olivine-saturated liquids (Helz & Thornber, 1987), thermal equilibration of
540 a hot olivine crystal with a cooler carrier melt drives the crystallization of a zoned
541 olivine rim from the melt inclusion, causing the MgO content of the melt inclusion
542 to drop to match that of the carrier melt (Fig. 3a). This zoned olivine rim begins to
543 re-equilibrate with the host crystal, and, in turn, the melt inclusion re-equilibrates
544 with the changing rim composition (Danyushevsky et al., 2000). The melt inclusion
545 loses FeO by diffusion to achieve Mg# equilibration with the host olivine follow-
546 ing the large initial drop in MgO during cooling. As the MgO content of the melt
547 inclusion is a function of the temperature, FeO diffusion is countered by MgO dif-
548 fusion in the opposite direction, which is sequestered by further post-entrapment
549 crystallization of olivine on the wall of the melt inclusion.

550 This FeO-loss process accounts for the negative correlation between melt in-
551 clusion FeO_T contents and the amount of PEC (Fig. 3d). For a given amount of
552 PEC, F8 melt inclusions have lower FeO_T contents and display a smaller degree
553 of Mg# disequilibrium with their olivine host than the vast majority of literature
554 data (Fig. 3b, d). It is important to note that methods calculating the amount of
555 PEC based on the degree of Mg# disequilibrium between the melt inclusion and the
556 host crystal (e.g., Tucker et al., 2019; Neave et al., 2017) will significantly under-
557 estimate the true amount of PEC in melt inclusions where extensive FeO-loss has
558 occurred compared to the Petrolog3 method used here where the user specifies an
559 initial FeO_T content. For example, the May-18 melt inclusions with $\text{Fo} > 85$ have lost
560 sufficient quantities of FeO by diffusive re-equilibration such that their Mg#s are in
561 equilibrium with the composition of the host olivine. Thus, methods based on Mg#
562 comparisons would indicate that these melt inclusions have experienced very minor
563 amounts of PEC. However, their FeO contents lie ~ 4 wt% below the composition
564 of co-erupted matrix glasses, indicating that their compositions have been heavily
565 altered by the PEC process (Fig. 3a).

566 The higher degrees of diffusive FeO-loss for a given amount of PEC for F8
 567 melt inclusions compared to literature data (Fig. 3d) indicates that there was a
 568 longer time lag between the entrainment of crystals into cooler melts and their
 569 eventual eruption. Danyushevsky et al. (2002) quantitatively model Fe-Mg re-
 570 equilibration to estimate this time lag: their Fig. 4c shows that a melt inclusion
 571 with a $\sim 50 \mu\text{m}$ radius that has experienced $\Delta T=100\text{--}150^\circ\text{C}$ and undergone FeO loss
 572 at $T=1150\text{--}1200^\circ\text{C}$ achieves 98% equilibrium in ~ 2 years. These extents of cooling
 573 and temperatures of re-equilibration are representative of F8 inclusions. However,
 574 Danyushevsky et al. (2002) assume isotropic diffusion of Fe through the host olivine
 575 crystal with $D_{\text{Fe, Mg}} \sim 3\text{--}6 \times 10^{-17} \text{ m}^2/\text{s}$ at $1150\text{--}1200^\circ\text{C}$. In reality, FeO loss will be
 576 dominated by diffusion along the fast c-direction in olivine ($D_{\text{Fe, Mg}} \sim 1\text{--}4 \times 10^{-16}$
 577 m^2/s for $\text{Fo}_{80\text{--}89}$, $T=1150\text{--}1200^\circ\text{C}$, and QFM to QFM+0.3; Chakraborty, 2010;
 578 Barth et al., 2019). Thus, complete re-equilibration could be achieved almost an
 579 order of magnitude faster, in a matter of months. Considering the substantial un-
 580 certainties in this method associated with the fact the model of Danyushevsky et
 581 al. (2002) does not account for diffusional anisotropy, and the fact the degree of
 582 re-equilibration is very sensitive to the choice of K_D (Fig. 3b), the FeO_T system-
 583 atics of melt inclusions within High-Fo olivines erupted on May 28th ($\sim 70\text{--}100\%$
 584 re-equilibration) indicate that entrainment into cooler carrier melts occurred approx-
 585 imately a month to a year prior to eruption.

586 5.2 Diffusive H_2O -loss

587 Given that H_2O in melt inclusions diffusively re-equilibrates over hours to days
 588 (Hartley et al., 2015; Le Voyer et al., 2014; Gaetani et al., 2012), the timescales in-
 589 ferred from Fe-Mg disequilibrium are more than sufficient for H_2O contents within
 590 F8 melt inclusions to be fully reset to the H_2O content of the melt which carried
 591 them to the site of the eruption. This re-equilibration accounts for the remarkably
 592 uniform H_2O contents of F8 melt inclusions in each sample, despite substantial
 593 variation in the concentration of other incompatible elements (e.g., Na_2O ; Fig. 5a).
 594 The approximately constant H_2O contents in melt inclusions from each sample in-
 595 dicates that F8 carrier melts erupted in late May had H_2O contents of 0.29 wt%,
 596 while those erupted in July and August had slightly lower H_2O contents ($\sim 0.22\text{--}0.23$
 597 wt%). These carrier melts are relatively H_2O -poor compared to the composition

598 of previously-erupted Kilauean melts (inferred from published melt inclusion data;
599 Fig. 5). The presence of more H₂O-poor carrier melts in 2018 likely results from the
600 extensive mixing of magmas which had partially degassed their H₂O at the summit
601 lava lake with undegassed melts within the plumbing system between 2008 and 2018
602 (similar to the mechanism proposed for Puna Ridge magmas by Dixon et al., 1991).

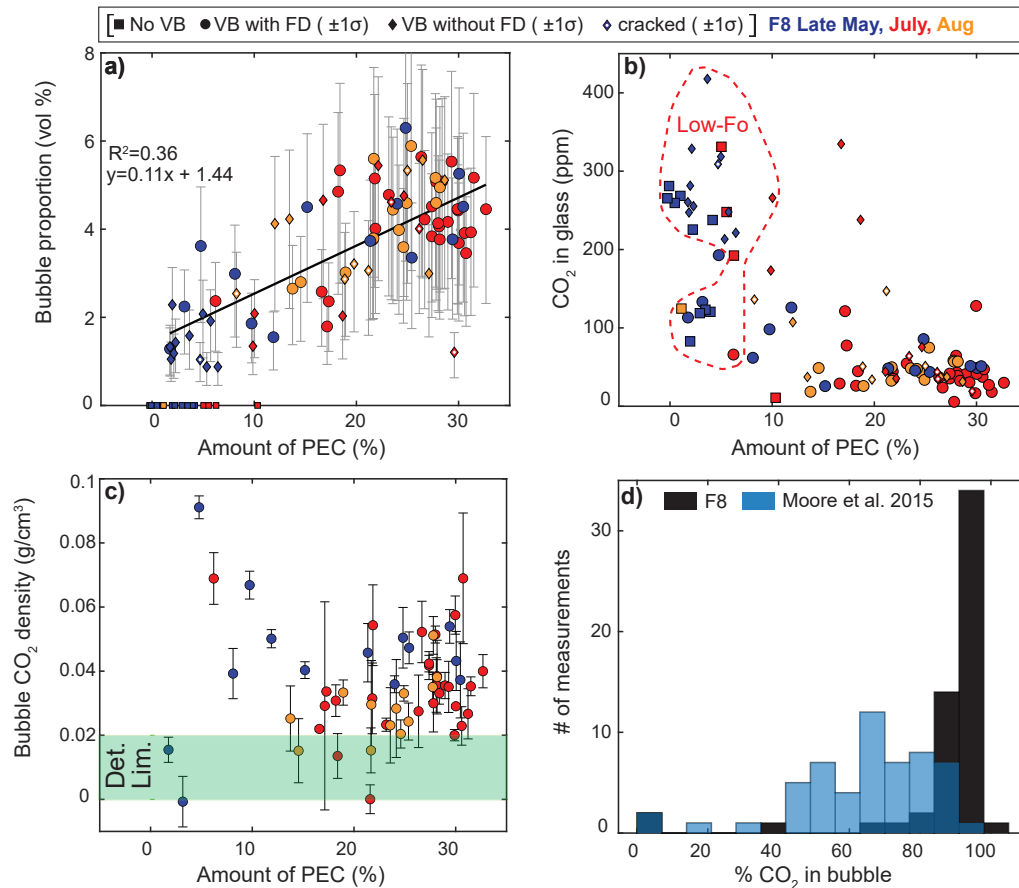


Figure 4. Vapor bubble and melt inclusion CO₂ systematics. a) There is a positive correlation between the volume proportion of the vapor bubble (VB) and the amount of PEC. Only melt inclusions which have experienced <10% PEC are bubble-free. Error bars show the 1σ errors associated with estimating bubble volume proportions from 2D images (-45% and +37% Tucker et al., 2019). b) With increasing amounts of PEC, the amount of CO₂ within the glass phase of the melt inclusion declines. The highest glass CO₂ contents are observed in melt inclusions with no vapor bubbles (squares), and melt inclusion with bubbles that did not produce a FD (diamonds). In contrast, the vast majority of melt inclusions with low glass CO₂ contents have vapor bubbles which produced a FD (circles), or vapor bubbles without a FD that were hosted within cracked melt inclusions (diamonds with white dots). c) There is no correlation between the CO₂ density in vapor bubble measured using Raman Spectroscopy and the amount of PEC. Error bars show the $\pm 1\sigma$ deviation of three repeated measurements of each vapor bubble. The green bar shows our estimate of the detection limit (Det. Lim.) of Raman analyses based on the distribution of measured bubble densities. d) The black histogram shows the proportion of CO₂ held within the vapor bubble for F8 melt inclusions that produced a FD (mean=87%, median=93%). Estimates by Moore et al. (2015) for Kīlauean melt inclusions from the 1959 and 1960 eruptions are also shown.

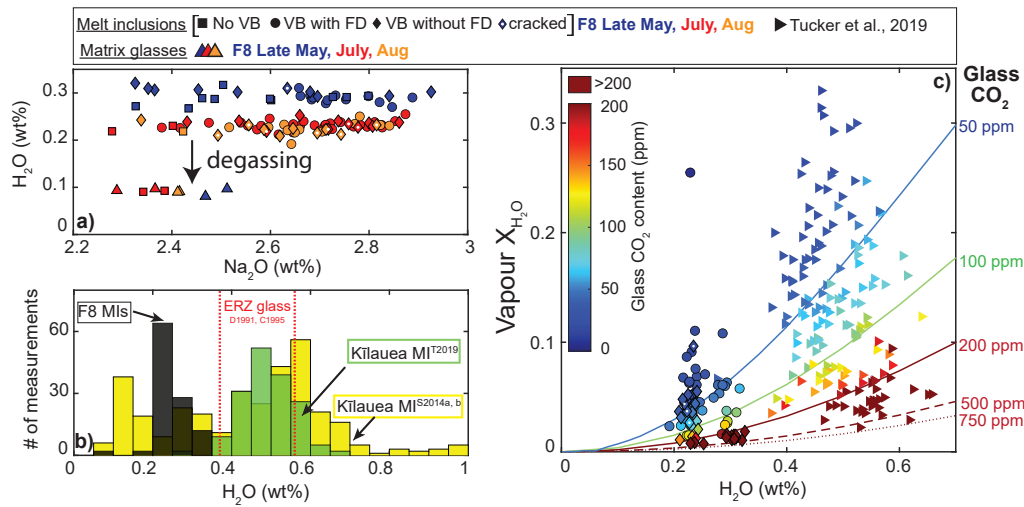


Figure 5. H₂O systematics of F8 melt inclusions relative to literature data from Kilauea. a) F8 melt inclusion H₂O contents are remarkably constant within each sample, despite substantial variations in Na₂O. This indicates that melt inclusion H₂O contents were reset by diffusive re-equilibration with their carrier liquid. The precision of SIMS measurements ($\pm 1.5\%$) is smaller than the symbol size, so error bars are not shown. b) F8 melt inclusions have lower H₂O contents than the majority of Kilauean melt inclusions measured by Sides, Edmonds, Maclennan, Swanson, and Houghton (2014); Sides, Edmonds, Maclennan, Houghton, et al. (2014) (yellow histogram) and almost all of the melt inclusions measured by Tucker et al. (2019). H₂O contents from submarine ERZ glasses with 7–16 wt% H₂O from Dixon et al. (1991); Clague et al. (1995) are shown with red dashed lines. c) Relationship between the molar fraction of H₂O in the vapor phase (X_{H_2O}) and the melt H₂O content for five different melt CO₂ contents (50, 100, 200, 500 and 750 ppm; using VolatileCalc-Basalt; Newman and Lowenstern, 2002). X_{H_2O} ratios for the co-existing vapor in equilibrium with the measured concentration of CO₂ and H₂O in the melt phase of the bubble-bearing inclusions from this study and Tucker et al. (2019) (triangles) are overlain, with symbols colored by the CO₂ content of the glass phase. The relatively low H₂O contents of F8 melt inclusions mean that X_{H_2O} is generally < 0.1 . However, a number of inclusions from Tucker et al. (2019) with glass CO₂ contents < 100 ppm have much higher X_{H_2O} ratios. This causes the CO₂ densities predicted using the EOS method to fall below the trend line defined by F8 melt inclusions on Fig. 8a.

5.3 PEC and melt-vapor CO₂ partitioning

It is well recognized that extensive PEC drives the growth of a CO₂-rich vapor bubble (Steele-Macinnis et al., 2011; Sides, Edmonds, MacLennan, Houghton, et al., 2014; Sides, Edmonds, MacLennan, Swanson, & Houghton, 2014; Aster et al., 2016; MacLennan, 2017). Thus, studies measuring only the CO₂ in the melt phase using SIMS or FTIR will yield spuriously low entrapment depths for melt inclusions which have undergone extensive PEC (e.g., Sides, Edmonds, MacLennan, Houghton, et al., 2014). Our concurrent measurements of CO₂ in the melt and bubble phase of a large number of melt inclusions which have experienced a wide range of PEC amounts (Fig. 3c-d) provides a unique opportunity to interrogate the various processes causing CO₂ to partition into the vapor bubble.

To investigate the effects of compositional changes in the melt inclusion associated with PEC, we use the CO₂ solubility model of Shishkina et al. (2014):

$$\ln[\text{CO}_2] = 1.15\ln(P) + 6.71\Pi^* - 1.345 \quad (4)$$

Where [CO₂] is the concentration of CO₂ in ppm, and P is the pressure in MPa. The Π^* term accounts for the compositional dependence on CO₂ solubility, expressed in terms of the cation fractions of 7 major element species:

$$\Pi^* = \frac{\text{Ca}^{2+} + 0.8\text{K}^+ + 0.7\text{Na}^+ + 0.4\text{Mg}^{2+} + 0.4\text{Fe}^{2+}}{\text{Si}^{4+} + \text{Al}^{3+}} \quad (5)$$

We calculate the change in Π^* during PEC, $\Delta \Pi^*$, by subtracting the Π^* value of the PEC-corrected major element composition of each melt inclusion from the Π^* value of the measured composition. $\Delta \Pi^*$ becomes progressively more negative with increasing amounts of PEC, showing that CO₂ becomes progressively less soluble (red dots; Fig. 6b, see also MacLennan, 2017). Changes in Π^* are dominated by a decrease in X_{Mg} , and increase in X_{Si} and X_{Al} resulting from the crystallization of olivine on the walls of the inclusion. These changes are partially counteracted by an increase in X_{Ca} (as Ca is incompatible in olivine). To quantify the magnitude of this drop in Π^* in terms of CO₂ partitioning between the melt and bubble, we consider the 8 melt inclusions which have experienced >30% PEC (all of which contain bubbles which produce a FD). The mean Π^* value of the measured compositions of

630 these melt inclusions is 0.33, while the mean Π^* of their PEC-corrected compositions
631 is 0.39 ($\Delta \Pi^* = -0.068$). For $P = 0.76$ kbar, which is the average entrapment pressure
632 for the PEC-corrected compositions of these melt inclusions calculated using equa-
633 tion 4, CO_2 solubility drops by ~ 192 ppm. As melts at Kīlauea are CO_2 saturated
634 at crustal storage depths (Gerlach et al., 2002), this extra CO_2 will partition into
635 the vapor bubble.

636 However, the mean amount of CO_2 sequestered within the vapor bubbles of
637 these 8 melt inclusions is 657 ± 231 ppm (calculated using equation 1). This reflects
638 three additional processes which enhance CO_2 partitioning into the bubble during
639 PEC. Firstly, the crystallization of olivine, which contains negligible quantities of
640 CO_2 , drives up the total concentration of the CO_2 in the remaining melt by a factor
641 of 1 plus the amount of PEC (1.3 to $1.33\times$ for these 8 melt inclusions). As men-
642 tioned above, because Kīlauea melt inclusions are CO_2 saturated (Gerlach et al.,
643 2002), this excess partitions into the bubble (mean 145 ppm, up to 230 ppm CO_2).
644 Secondly, the preferential contraction of the melt phase relative to the olivine during
645 thermal re-equilibration leads to a reduction in the volume of the melt phase. This
646 is enhanced by the third process; the crystallization of denser olivine on the rim of
647 the melt inclusion. A drop in the internal pressure of the melt inclusion causes the
648 CO_2 solubility to decrease further, driving more CO_2 into the vapor bubble (equa-
649 tion 5). Evidence for these volume changes is provided by the correlation between
650 the amount of PEC and the volume of the vapor bubble (Fig. 4a), as well as the
651 observation that all melt inclusions without a vapor bubble have experienced $< 10\%$
652 PEC (Fig. 4a), while all melt inclusions that have experienced $> 10\%$ PEC have a
653 vapor bubble.

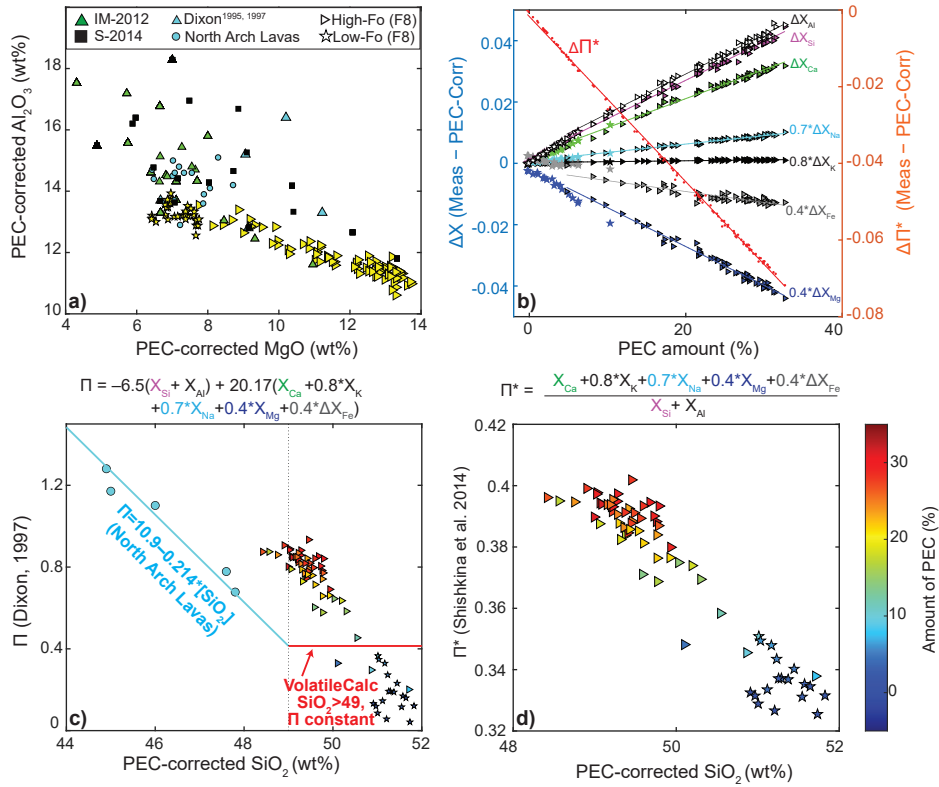


Figure 6. Evaluating the compositional sensitivity of CO₂ solubility. a) Comparison of the MgO vs. Al₂O₃ systematics of PEC-corrected F8 inclusions to the glass compositions used to calibrate each solubility model. The North Arch lavas which define the simplified Π vs. SiO₂ relationship presented in Dixon (1997) and implemented in VolatileCalc-Basalt (Newman & Lowenstern, 2002) are also shown (blue circles). The MagmaSat dataset (Ghiorso & Gualda, 2015) includes the experiments in the calibration datasets of Shishkina et al. (2014), Iacono-Marziano et al. (2012) and Dixon et al. (1995) (so is not shown, as it would cover all these symbols). b) ΔX (triangle and star symbols) and ΔΠ* (red dots Shishkina et al., 2014) for F8 melt inclusions plotted against the amount of PEC. ΔX and ΔΠ* were calculated by subtracting the values of X and Π* for PEC-corrected melt inclusions from the values of X and Π* for measured compositions. For example, inclusion LL8.156 has experienced 33% PEC, and has a PEC-corrected MgO content of 13.5 wt% and a measured MgO content of 5.4 wt%. Thus, ΔX_{MgO} is strongly negative. c) The compositional parameter Π of Dixon (1997) calculated for PEC-corrected F8 melt inclusion compositions varies substantially with SiO₂, following an offset trend to that defined by North Arch Glasses (Dixon et al., 1997, blue dots and linear regression). VolatileCalc-Basalt effectively treats all melt inclusions with >49 wt% SiO₂ as if Π is constant (red line). d) The compositional parameter Π* from Shishkina et al. (2014), and therefore the solubility of CO₂, is significantly higher for High-Fo melt inclusions (which have the highest PEC-corrected MgO, and lowest SiO₂ and Al₂O₃ contents). The color of the symbols for F8 melt inclusions in c) and d) represents the amount of PEC.

654 Overall, changes in melt chemistry, the incompatible behaviour of CO₂, and a
655 drop in the internal pressure of the melt inclusion accounts for the rapid decrease in
656 glass CO₂ contents with increasing PEC (Fig. 4b). Our concurrent measurements of
657 glass and bubble CO₂ provide the first opportunity to see through these convoluting
658 effects of PEC to robustly determine total CO₂ contents, and therefore entrapment
659 depths of Kīlauean melt inclusions. To account for the uncertainty regarding the
660 amount of CO₂ held within bubbles that did not produce a FD (diamond symbols),
661 particularly those hosted within cracked olivines (diamond symbols with white dot),
662 we only calculate total CO₂ contents and entrapment depths for melt inclusions
663 which had no bubble, or a bubble that produced a FD. These total CO₂ were cor-
664 rected for the incompatible behaviour of CO₂ during PEC to determine the total
665 CO₂ content at the point of melt inclusion entrapment.

666 Total PEC-corrected CO₂ contents in melt inclusions hosted within High-Fo
667 olivines are offset to significantly higher values compared to those hosted within
668 Low-Fo olivines (Fig. 7a), indicating that these two olivine populations crystal-
669 lized at distinct depths within Kīlauea’s plumbing system. It is also interesting to
670 compare our total CO₂ contents to previously published data on Kīlauean melt
671 inclusions. Although these studies investigate products from different eruptions,
672 the apparent stability in the geometry of Kīlauea’s plumbing system since at least
673 the 1950s (Helz et al., 2014; Poland et al., 2015; Eaton & Murata, 1960) means
674 such comparisons are still useful (and particularly relevant for studies of the 1959–
675 1960 eruptive period, where activity at the summit was followed by a large LERZ
676 eruption; e.g., Tuohy et al., 2016; Moore et al., 2015; Sides, Edmonds, Maclen-
677 nan, Houghton, et al., 2014; Sides, Edmonds, Maclennan, Swanson, & Houghton,
678 2014) . Unsurprisingly given our findings that ~90% of CO₂ is held within the va-
679 por bubble (Fig. 4d), CO₂ contents in F8 melt inclusions are significantly higher
680 than measurements of just the glass phase by Sides, Edmonds, Maclennan, Swanson,
681 and Houghton (2014); Sides, Edmonds, Maclennan, Houghton, et al. (2014) (Fig.
682 7c). F8 melt inclusions are also offset to higher CO₂ contents than experimentally-
683 rehomogenized melt inclusions (Tuohy et al., 2016, Fig. 7d). Tuohy et al. (2016)
684 note similar offsets between their measurements and Raman reconstructions of bub-
685 ble CO₂ by Moore et al. (2015) in the same sample set. They suggest that their
686 analyses may have been biased towards melt inclusions with smaller bubbles that

687 fully disappear upon heating, lower pressure inclusions that do not fracture during
688 heating, and larger inclusions that can be analysed by FTIR.

689 Interestingly, our distribution of total CO₂ contents for melt inclusions which
690 possessed bubbles are indistinguishable using the Kolmogorov-Smirnov (KS) test
691 (p=0.1) from the CO₂ contribution of just the vapor bubbles in melt inclusions
692 from the 1959 and 1960 eruptions of Kilauea (Moore et al., 2015, Fig. 7e). This
693 demonstrates that in olivine populations which have experienced extensive PEC,
694 measurements of glass CO₂ contents are of subordinate importance to measurements
695 of bubble CO₂. Furthermore, the contribution of CO₂ from the melt phase for the
696 majority of High-Fo melt inclusions from F8 is entirely overwhelmed by the errors
697 on the amount of CO₂ in the bubble associated with estimating bubble volume pro-
698 portions from 2D images. However, it is worth noting that only measuring CO₂ in
699 vapor bubble would have failed to identify the population of Low-Fo olivines which
700 host almost all of their CO₂ within the glass phase. Thus, we suggest that future
701 studies use a small number of SIMS or FTIR analyses of melt inclusions, combined
702 with EPMA analyses of host crystals and melt inclusions, to determine the relation-
703 ship between glass and bubble CO₂ contents and the amount of PEC in different
704 subpopulations of melt inclusions. If the vast majority of CO₂ in a given population
705 is held in the vapor bubble, a limited analytical budget would be better spent accu-
706 rately measuring bubble volumes (using MicroCT or 3D Raman mapping; Pamukcu
707 et al., 2013; Venugopal et al., 2020) to combine with Raman measurements of CO₂
708 density in the rest of the sample set, instead of precisely quantifying the insignificant
709 amount of CO₂ held within the glass phase using SIMS or FTIR.

710 Importantly, we also observe that the distribution of total CO₂ contents in
711 bubble-bearing melt inclusions is significantly higher than bubble-free melt inclu-
712 sions (Fig. 7b). This result invalidates the approach of preferentially targeting
713 bubble-free melt inclusions to avoid having to account for CO₂ within the vapor
714 bubbles (e.g., Helo et al., 2011; Esposito et al., 2011) in systems where erupted crys-
715 tals have experienced extensive PEC prior to eruption. Crucially, analysis of only
716 bubble-free melt inclusions by SIMS or FTIR, or analyses of just vapor bubbles us-
717 ing Raman, would have failed to identify that crystals are supplied from two distinct
718 storage regions within Kilauea's plumbing system.

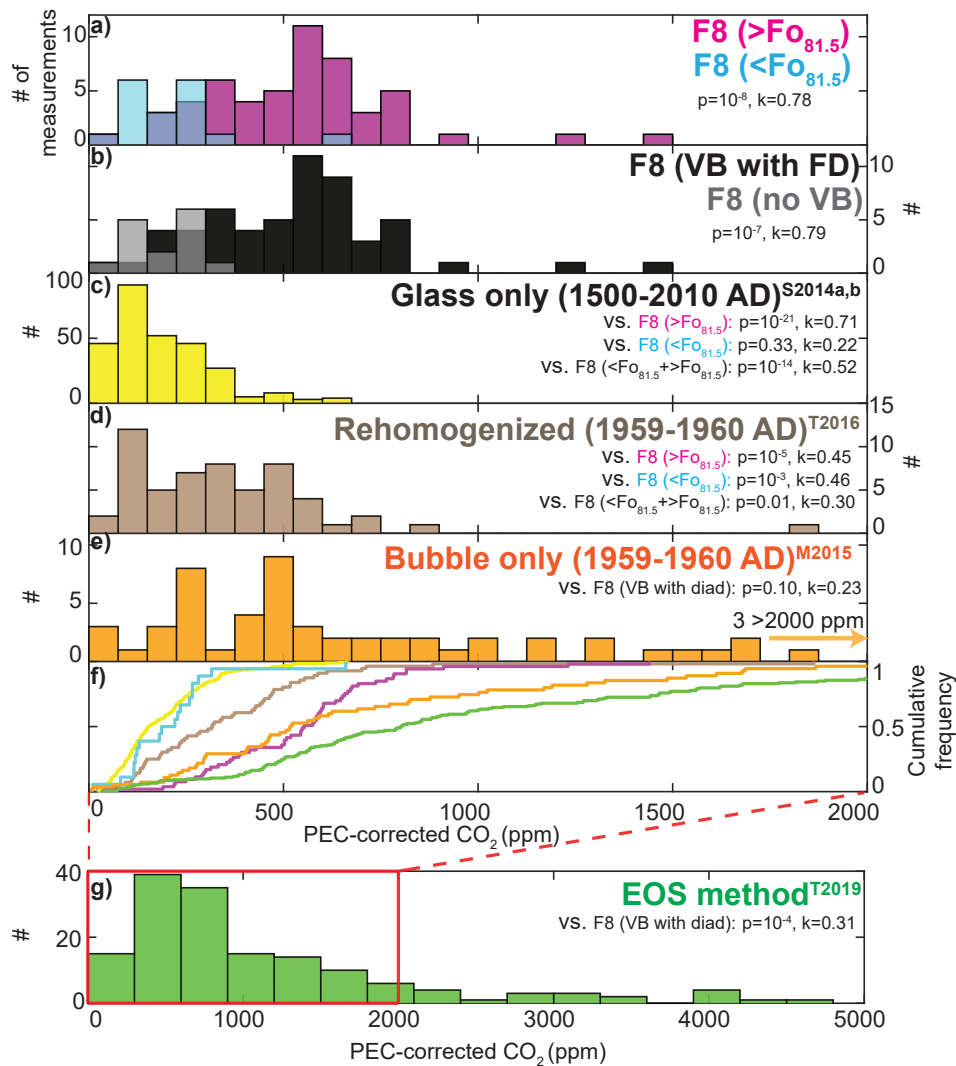


Figure 7.

719 **Caption Fig. 7** Histograms of melt inclusion CO₂ contents from this study and
 720 the literature (all corrected for the effects of PEC). a) Total CO₂ contents (bub-
 721 ble+glass) for High and Low-Fo melt inclusions are statistically distinguishable at
 722 $p=0.05$ using the Kolmogorov Smirnov (KS) test (p value and test statistic k shown
 723 on the figure). b) Similarly, melt inclusions which contain a vapor bubble (VB) with
 724 a FD have significantly higher total CO₂ contents than bubble-free melt inclusions.
 725 c) Melt inclusion CO₂ contents from a suite of eruptions at Kilauea between 1500
 726 and 2008 AD where only the glass phase was measured (Sides, Edmonds, Maclennan,
 727 Swanson, & Houghton, 2014; Sides, Edmonds, Maclennan, Houghton, et al.,
 728 2014). d) CO₂ contents of experimentally-homogenized melt inclusions from the

729 1959 Kīlauea Iki and 1960 Kapoho eruptions (Tuohy et al., 2016). e) Bubble CO₂
730 contents from Moore et al. (2015) in the same suite of samples as in d). For consis-
731 tency, these bubble CO₂ contents were corrected for PEC using the average amount
732 of PEC reported by Tuohy et al. (2016) (13%). f) Cumulative distribution plots
733 for these datasets. g) Total inclusion CO₂ contents from Tucker et al. (2019) where
734 the contribution from bubble CO₂ was estimated using the EOS method (excluding
735 inclusions with bubble volumes >8% that the authors suggest were co-entrapped).
736 35 melt inclusions have CO₂ >1500 ppm. Note the change in x axis scale from plots
737 a-f). For literature data, all melt inclusions are shown, as Fo contents were not re-
738 ported by Moore et al. (2015), and matrix glass Mg#s were not reported in Tucker
739 et al. (2019), so it was not possible to classify data based on the degree of olivine-
740 melt disequilibrium as for F8 samples.

741 **5.4 Analytical versus theoretical constructions of vapor bubble CO₂**

742 In contrast to the good agreement between our estimates of total CO₂ con-
743 tents from combined SIMS and Raman measurements from F8 and the bubble-only
744 measurements of Moore et al. (2015), the total CO₂ contents estimated by Tucker
745 et al. (2019) for a range of Kīlauean eruptions using the EOS method are displaced
746 to significantly higher values (Fig. 7g). To assess the cause of this discrepancy, we
747 follow the EOS method they describe to calculate CO₂ bubble densities for F8 melt
748 inclusions to compare to our Raman measurements. The simplification of the Dixon
749 (1997) solubility model implemented in the excel workbook VolatileCalc (hereafter
750 VolatileCalc-Basalt Newman & Lowenstern, 2002) was used to calculate the internal
751 pressure of the melt inclusion based on the measured SiO₂, CO₂ and H₂O contents
752 of the glass phase. The pure CO₂ EOS of Span and Wagner (1996) implemented in
753 Python3 through CoolProp (Bell et al., 2014) was used to calculate the CO₂ den-
754 sity at this internal pressure and 725 °C, which was the presumed glass transition
755 temperature of Tucker et al. (2019) based on Ryan and Sammis (1981). The Duan
756 and Zhang (2006) EOS utilized by Tucker et al. (2019) yields identical densities to
757 the fourth decimal place (see Supporting Information Fig. S11). The more signifi-
758 cant source of error involves the choice of the glass transition temperature. This is
759 fixed at 725 °C in Tucker et al. (2019) and 825 °C in Moore et al. (2015)(dashed
760 and solid magenta line; Fig. 8a) for simplicity, but in reality, varies as a function of

761 cooling rate and melt viscosity (and, by extension, melt composition; Giordano et
 762 al., 2005; MacLennan, 2017). The average glass transition temperatures predicted by
 763 the bubble-growth python code MIMiC (which uses the model of Giordano et al.,
 764 2005; Rasmussen et al., 2020) for bubble-bearing F8 melt inclusions for cooling rates
 765 of 10 °C/s is 680 °C (dotted magenta line; Fig. 8a). Following Tucker et al. (2019),
 766 we multiply the density obtained from the pure-CO₂ EOS by the mole fraction of
 767 CO₂ (X_{CO_2}) in the vapor phase determined in VolatileCalc (Newman & Lowenstern,
 768 2002). This correction neglects the non-ideal mixing of H₂O and CO₂ at magmatic
 769 temperatures compared to the use of a mixed H₂O-CO₂ EOS (e.g., Moore et al.,
 770 2015) but is probably a reasonable approximation for relatively dry systems such as
 771 Kilauea (Fig. 5a-b).

772 The dominant control of the glass CO₂ content on the internal pressure of the
 773 inclusion in relatively anhydrous melts, and the positive relationship between the in-
 774 ternal pressure and ρ_{CO_2} from the EOS evaluated at a constant temperature, means
 775 that predicted ρ_{CO_2} values increase with increasing glass CO₂ contents (Fig. 8a).
 776 Predicted CO₂ densities from Tucker et al. (2019) plot on or below the quadratic fit
 777 through the EOS predictions for F8 melt inclusions at 725 °C (magenta solid line),
 778 because of the higher values of X_{H_2O} (and thus lower X_{CO_2}) for a number of melt
 779 inclusions which possess high glass H₂O, but low glass CO₂ contents (Fig. 5c). How-
 780 ever, unlike the predictions from the EOS method, there is no correlation between
 781 ρ_{CO_2} measured using Raman spectroscopy and glass CO₂ contents ($R^2=0.11$). In-
 782 terestingly, all melt inclusions with >200 ppm CO₂ in the glass have vapor bubbles
 783 which did not produce a FD (diamond symbols; Fig. 8a), indicating that their CO₂
 784 densities were below the detection limit of Raman Spectroscopy ($\sim 0-0.02$ g/cm³;
 785 green bar in Fig. 4c). It seems implausible that these bubbles could possess the high
 786 CO₂ densities predicted by the EOS ($\rho_{CO_2} > 0.2$ g/cm³) and fail to produce a FD.
 787 Furthermore, melt inclusions with $\rho_{CO_2} > 0.2$ g/cm³ will consist of an outer shell of
 788 liquid CO₂, and an inner sphere of vapor CO₂ at room temperature ($\sim 21-22$ °C).
 789 For $\rho_{CO_2}=0.4$ g/cm³, this liquid phase will comprise 26% of the radius of the bub-
 790 ble, and the motion of the inner sphere of vapor because of Brownian motion would
 791 be readily observable under an optical microscope. Yet, we observe no two-phase
 792 bubbles, and there are no reports of two-phase bubbles in the Kilauean literature.

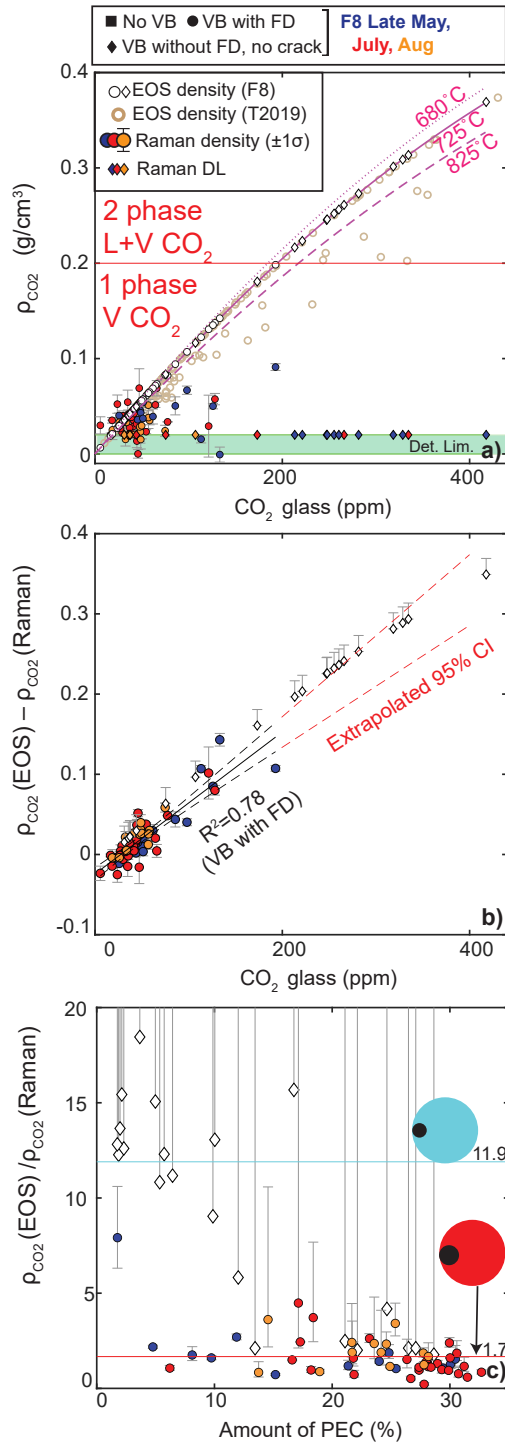


Figure 8. Comparisons of bubble CO₂ densities calculated using the EOS with those measured by Raman Spectroscopy. a) Calculated ρ_{CO_2} correlates strongly with glass CO₂. Bubbles within F8 melt inclusions are shown as white circles and diamonds (FD and no FD), bubbles within melt inclusions from Tucker et al. (2019) are shown as beige hollow circles. Magenta lines shows quadratic fits through calculated bubble densities for F8 melt inclusions for the EOS evaluated at 680°C, 725°C and 825°C. A number of inclusions with low inclusion CO₂ contents and high H₂O contents from Tucker et al. (2019) lie below this line, because of their higher X_{H_2O} values (Fig. 5c). Measured ρ_{CO_2} in this study are shown as colored circles, with error bars showing the 1σ of repeated acquisitions of each bubble. Colored diamonds (no FD, not cracked) are plotted at 0.02 g/cm³ (the presumed detection limit of Raman Spectroscopy; see Fig. 4c). b) The absolute discrepancy between predicted and measured ρ_{CO_2} , $\Delta \rho_{CO_2}$, correlates strongly with glass CO₂ content. The 95% confidence interval on a linear regression for measured bubble densities is shown with red dotted lines. Bubbles which did not produce a FD lie within error of the extrapolated confidence interval (assuming $\rho_{CO_2}=0.02$ g/cm³). c) To allow comparison with bubble growth models in Fig. 9, the discrepancy between EOS methods and Raman measurements are shown as a factor (as above, VB without a FD assumed to contain 0.02 g/cm³). The proportion of the total bubble volume grown during quench for the High- and Low-Fo models shown in Fig. 9 are shown with red and cyan lines respectively. Error bars in b) and c) for VB with FD show the 1σ uncertainty of repeated Raman measurements, and those for VB without FD are calculated for DL between 0–0.02 g/cm⁻³ (hence they extend to infinity in c).

793 The fundamental tenet of the EOS method used by Tucker et al. (2019) is that
794 CO₂ continues to partition between the vapor bubble and the melt until the bubble
795 stops growing at the glass transition temperature. However, during syn-eruptive
796 quenching, the strong temperature dependence of CO₂ diffusivity means that the
797 diffusion of CO₂ from the melt into the bubble may cease before the bubble reaches
798 its final volume (Anderson and Brown, 1993). Continued bubble growth without
799 concurrent diffusion causes the density of CO₂ within the bubble to drop below that
800 predicted from the EOS (Aster et al., 2016; Moore et al., 2015; Maclennan, 2017).
801 Non-equilibrium bubble expansion has been proposed to account for the presence
802 of vapor bubbles in Icelandic melt inclusions with CO₂ concentrations below the
803 detection limit of Raman Spectroscopy (Neave et al., 2014).

804 The discrepancy between EOS predictions and Raman measurements ($\Delta \rho_{CO_2}$)
805 increases linearly with glass CO₂ content ($R^2=0.75$; shown as an absolute discrep-
806 ancy, Fig. 8b) and decreases with the amount of PEC (shown as a factor, Fig. 8c).
807 Melt inclusions containing bubbles without a FD lie within the confidence interval
808 of the regression through bubbles which produced a FD if the Raman detection
809 limit (0.02 g/cm³) is subtracted from CO₂ densities calculated from the EOS (Fig.
810 8b). To investigate these correlations, we assess the relative contribution of bubble
811 growth at high magmatic temperatures during PEC and ascent (where CO₂ diffusion
812 and bubble growth are coupled) compared to bubble growth during quench (where
813 CO₂ diffusion is temperature-limited, and therefore decoupled from the mechanical
814 expansion of the bubble).

815 We model melt inclusions from the point of entrapment to the glass transition
816 temperature using the model of Maclennan (2017; Fig. 9). Quench rates of 10°C/s
817 were used based on video footage of the sampling and quenching of the Aug-18 sam-
818 ple; ~40 s elapsed between the sample being pulled from the channel (~1150°C)
819 and becoming brittle at the glass transition temperature (~725 °C Tucker et al.,
820 2019). At these cooling rates, there is negligible transfer of CO₂ from the melt to
821 the bubble during syn-eruptive quenching. Two end-member cooling histories were
822 modelled. The red melt inclusion in Figure 9a experienced large amounts of cooling
823 ($\Delta T=150^\circ C$) and PEC at high magmatic temperatures and pressures, representa-
824 tive of the PT path followed by melt inclusions hosted within the most forsteritic
825 olivines. The blue melt inclusion in Figure 9b experiences no cooling and post-

826 entrapment crystallization prior to ascent and syn-eruptive quenching, representative
827 of Low-Fo melt inclusions which form in carrier melts with similar temperatures to
828 the ones in which they were erupted.

829 The High-Fo melt inclusion (red) grows a considerable proportion of its final
830 bubble volume (58%) during PEC at high magmatic temperatures (square to star
831 symbol; Fig. 9a). The diffusion of CO₂ into this growing bubble causes the CO₂
832 content of the melt phase to drop rapidly (Fig. 9c). During syn-eruptive quenching,
833 there is no further CO₂ diffusion between the melt and bubble (Fig. 9c). This stage
834 of bubble growth accounts for 42% of the final volume, with ρ_{CO_2} decreasing from
835 0.10 to 0.06 g/cm³ (Fig. 9a, d). As the EOS method effectively predicts the density
836 of CO₂ in the vapor bubble prior to the final, quench-induced stage of bubble ex-
837 pansion, the EOS method overpredicts the CO₂ density by a factor of 1.7× in this
838 example. This lies well within the deviation between measured and predicted CO₂
839 contents for High-Fo F8 melt inclusions which have experienced >10% PEC (red line
840 on Fig. 8c). In this case, the proportion of the bubble grown at high temperatures
841 will be substantially greater, as the model of Maclennan (2017) does not account for
842 the FeO-loss process, which greatly increases the amount of PEC for a given ΔT .
843 The volume of the bubble grown during syn-eruptive quench is determined by the
844 difference between the temperature at the initiation of syn-eruptive quenching, and
845 the glass transition temperature, so is almost constant for different PT paths. In
846 contrast, with increasing amounts of PEC, the volume of the bubble grown at high
847 temperatures gets progressively larger, so the relative expansion of the bubble during
848 quench (and therefore the change in CO₂ density) gets progressively smaller. For
849 example, in models with $\Delta T=200^\circ\text{C}$ instead of $\Delta T=150^\circ\text{C}$, the amount of PEC
850 increases from 18% to 25%, and the proportion of the bubble grown at high temper-
851 ature increases from 58% to 68%. In turn the bubble density drops from only 0.073
852 to 0.052 g/cm³ during syn-eruptive quenching (so the EOS method would only over
853 predict by a factor of $\sim 1.4\times$).

854 In contrast, the Low-Fo melt inclusion (blue) grows a very small proportion of
855 its total bubble volume at high temperatures (10%), with 90% of the final bubble
856 volume growing upon quench (Fig. 9b). Substantial bubble expansion upon quench
857 without concurrent CO₂ diffusion causes ρ_{CO_2} to drop substantially (Fig. 9d). Ef-
858 fectively, the EOS method calculates the density of the bubble at the initiation of

859 the quench stage ($\rho_{CO_2}=0.205$ g/cm³; star symbol), while the true bubble density
860 is $11.9\times$ lower ($\rho_{CO_2}=0.021$ g/cm³; circle symbol), close to the detection limit of
861 Raman spectroscopy. This calculated discrepancy is very similar to that for vapor
862 bubbles in Low-Fo inclusions which do not have Fermi diads (assuming the detection
863 limit= 0.02 g/cm³, cyan line, Fig. 8c).

864 In summary, the EOS substantially overestimates ρ_{CO_2} for melt inclusions
865 which have experienced small amounts of PEC and retain high CO₂ contents (Fig.
866 8b,c), because bubble growth in these melt inclusions is dominated by the quench-
867 ing process where there is no diffusion of CO₂ into the bubble. In contrast to these
868 very large discrepancies (factors of ~ 10), bubble densities in melt inclusions which
869 have experienced extensive PEC are broadly matched by the EOS method (within a
870 factor of ~ 2 ; Fig. 8c).

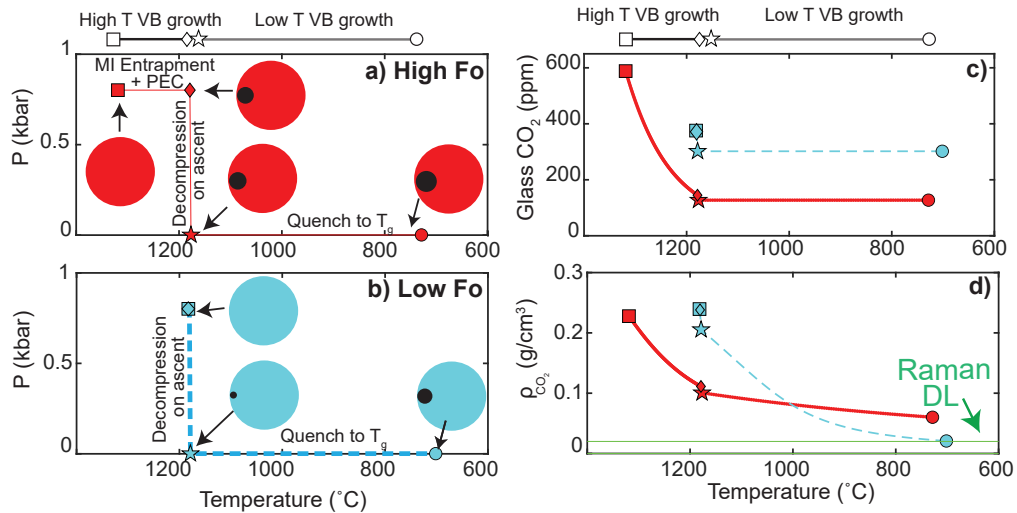


Figure 9. Model of CO₂ partitioning between the melt and bubble for PT scenarios representative of inclusions hosted within High and Low-Fo olivines (red and blue colors, respectively). a) The red melt inclusion experiences considerable cooling ($\Delta T=150^\circ\text{C}$) and post-entrapment crystallization at high temperatures and pressures (square to diamond symbol), driving the growth of a vapor bubble. This high temperature phase of bubble growth is accompanied by CO₂ diffusion from the melt to the bubble, causing the glass CO₂ content to drop substantially (c). This inclusion then ascends to the surface (diamond to star symbol), and experiences a second stage of vapor bubble growth during syn-eruptive quenching (star to circle symbol). b) The blue melt inclusion follows an end-member PT path representative of an inclusion hosted within a Low-Fo olivine. It experiences no cooling and post-entrapment crystallization at high temperature. A bubble only begins to grow during ascent to the surface, with 90% of the total bubble volume of this inclusion occurs during syn-eruptive quenching (star to circle). At the quenching rates of 10°C/s used in this model, there is negligible CO₂ transfer from the glass to the bubble during this low temperature phase of bubble growth. The large amount of bubble expansion without concurrent CO₂ diffusion causes the density of CO₂ in the vapor bubble to drop close to the detection limit of Raman Spectroscopy (green line, d), while the CO₂ of the glass phase remains unchanged (c).

871 These bubble-growth models show that the magnitude of the discrepancy be-
 872 between measured bubble densities and those predicted by the EOS relates to the
 873 proportion of the bubble grown during syn-eruptive quenching. In contrast, Tucker
 874 et al. (2019) suggest that Raman measurements may underestimate ρ_{CO_2} relative to

EOS methods because of the sequestration of significant quantities of CO₂ as thin
films of solid carbonate on bubble walls. Carbonate phases have been identified in a
number of melt inclusion vapor bubbles from subduction zone settings based on the
presence of a distinctive peak in the Raman spectra at $\sim 1090\text{ cm}^{-1}$ (Venugopal et
al., 2020; Moore et al., 2015). However, while Moore et al. (2015) report relatively
abundant carbonate phases in vapor bubbles from Seguam and Fuego, only four of
the 142 Kilauean vapor bubbles they examined contained carbonates, all of which
were hosted within a single olivine crystal. This suggests that vapor bubble carbon-
ates are significantly less common in H₂O-poor ocean island systems. We observe no
carbonate peaks in Raman spectra from F8 bubbles, nor during optical observations
made prior to the exposure of bubbles during polishing. Additionally, no carbonate
phases were identified during detailed examination of exposed bubble walls using
backscatter and secondary electron imaging, and Energy-Dispersive Spectroscopy
(EDS) maps on a FEG-SEM. These EDS maps reveal that bubble wall coatings with
a “dotted” appearance identified by Tucker et al. (2019) (see their Fig. 2F) consist
of Fe-Cu sulfides, rather than carbonates (see also Venugopal et al., 2020; Moore et
al., 2015; Wieser, Jenner, et al., 2020). Finally, even if carbonates in bubble walls
remained undetected, our observations regarding the systematic relationship between
PEC amounts, CO₂ contents, and the discrepancy between Raman measurements
and the EOS would necessitate that only bubbles hosted in melt inclusions which
had undergone negligible PEC contain carbonate phases.

5.5 Reconstructing Magma Storage Depths

Under the assumption that any reservoir from which a substantial proportion
of the crystal cargo was derived must also have supplied melt (in order to entrain
these crystals, and carry them to the surface), the depths of the main magma reser-
voirs supplying F8 can be estimated from melt inclusion entrapment pressures (for a
known crustal density). Entrapment pressures were calculated from PEC-corrected
total CO₂ and major element contents, and temperatures calculated using the MgO-
liquid thermometer of Helz and Thornber (1987) for PEC-corrected MgO contents.
As melt inclusion H₂O contents have been reset by diffusive re-equilibration, satu-
ration pressures were calculated assuming H₂O=0.5 wt%, based on the distribution
of measured H₂O contents in literature studies of Kilauean melt inclusions and un-

907 degassed submarine glasses from the ERZ (Fig. 5b; Sides, Edmonds, Maclennan,
 908 Houghton, et al., 2014; Sides, Edmonds, Maclennan, Swanson, & Houghton, 2014;
 909 Clague et al., 1995; Dixon et al., 1991; Tucker et al., 2019). Entrapment pressures
 910 for measured water contents are also shown in the Supplementary Information. En-
 911 trapment pressures were converted into magma storage depths assuming $\rho=2400$
 912 kg/m^{-3} (for consistency with modelling of the geodetic signals from the 2018 sum-
 913 mit collapse by Anderson et al., 2019). Initially, we consider melt inclusions with no
 914 vapor bubble, or a vapor bubble which produced a FD, due to the uncertainty in the
 915 CO_2 density of vapor bubbles which do not contain a FD.

916 Literature studies of Kīlauean melt inclusions have mostly calculated satura-
 917 tion pressures using the $\text{CO}_2\text{-H}_2\text{O}$ solubility model of Dixon et al. (1995) and Dixon
 918 (1997), implemented in the excel workbook VolatileCalc (Newman & Lowenstern,
 919 2002, e.g., Tuohy et al. 2016; Sides et al. 2014a, b; Moore et al., 2015; Tucker et al.,
 920 2019). VolatileCalc-Basalt uses a simplified relationship for the compositional de-
 921 pendence of CO_2 solubility expressed in terms of just the melt SiO_2 content, rather
 922 than the full compositional parameter Π which accounts for the abundance of seven
 923 cations (Dixon, 1997, Fig. 6c). In this simplification the parameter $X_{\text{CO}_3^{2-}}(P_0, T_0)$,
 924 which representing the solubility of CO_2 at 1200 °C and 1 bar for a specified fluid
 925 CO_2 fugacity in the thermodynamic expression of Dixon et al. (1995), is expressed
 926 as:

$$X_{\text{CO}_3^{2-}}(P_0, T_0) = 8.7 \times 10^{-6} - 1.7 \times 10^{-7}[\text{SiO}_2] \quad (6)$$

927 This relationship derives from the excellent linear correlation between Π and
 928 SiO_2 in a suite of lavas with 40–49 wt% from the North Arch Volcanic field (blue
 929 regression line; Fig. 6c; Dixon et al., 1997). However, extrapolation of Equation 6
 930 beyond 51.2 wt% SiO_2 returns a negative value for $X_{\text{CO}_3^{2-}}(P_0, T_0)$, which, in turn,
 931 predicts that the solubility of CO_2 is negative at all pressures. To avoid these ex-
 932 trapolation issues, VolatileCalc-Basalt does not let users enter a SiO_2 content >49
 933 wt%, so most studies simply calculate the CO_2 solubility for melts with >49 wt%
 934 SiO_2 using the expression for $\text{SiO}_2=49$ wt% (e.g., Tucker et al., 2019; Sides, Ed-
 935 monds, Maclennan, Houghton, et al., 2014; Sides, Edmonds, Maclennan, Swanson,
 936 & Houghton, 2014). Newman and Lowenstern (2002) suggest that this approxima-

937 tion should return accurate entrapment pressures for basaltic compositions with up
938 to 52 wt% SiO₂ contents. However, the simplified compositional parameter used in
939 VolatileCalc-Basalt is only valid for melt compositions which define the same tra-
940 jectories in Π vs. SiO₂ space as the North Arch Lavas. F8 melt inclusions which
941 have undergone >10% PEC are offset to substantially higher Π values at a given
942 SiO₂ (Fig. 6c), so VolatileCalc-Basalt underestimates the solubility of CO₂. Addi-
943 tionally, while F8 melt inclusions show a large drop in Π with increasing SiO₂, all
944 but four melt inclusions have SiO₂ >49 wt%, so are treated as if they had the same
945 composition in VolatileCalc-Basalt (red line; Fig. 6c). Thus, VolatileCalc-Basalt not
946 only underestimates CO₂ solubility, and therefore overestimates entrapment pres-
947 sures for F8 melt inclusions hosted in High-Fo olivines, it also neglects compositional
948 variations in CO₂ solubility within this suite (Fig. 6c).

949 To demonstrate the importance of evaluating the suitability of different solu-
950 bility models, we compare entrapment pressures from VolatileCalc-Basalt with the
951 models of Ghiorso and Gualda (2015), hereafter MagmaSat, Iacono-Marziano et
952 al. (2012) with hydrous coefficients, hereafter IM-2012, and Shishkina et al. (2014),
953 hereafter S-2014, using the open-source python tool VESIcal (Iacovino et al., 2020).
954 These three models utilize more than a decade of additional experiments on basaltic
955 compositions compared to the expressions implemented in VolatileCalc-Basalt. By
956 extension, these models are calibrated on a significantly larger compositional range
957 (Fig. 6a), so more effectively encapsulate variability in CO₂ solubility as a function
958 of melt composition.

959 Entrapment pressures for melt inclusions hosted in Low-Fo olivines from F8
960 calculated using VolatileCalc-Basalt, S-2014, and IM-2012 are statistically indistin-
961 guishable using the KS test at $p=0.05$ (Fig. 10a), likely because the major element
962 compositions of these melt inclusions lie within the calibration range of all four sol-
963 ubility models (Fig. 6a). MagmaSat returns slightly lower pressures, although these
964 are not statistically distinguishable ($p=0.1$ vs. S-2014). These slight discrepancies
965 likely reflect the differential treatment of mixing between H₂O and CO₂ fluids in
966 these different models (e.g., non-ideal mixing in MagmaSat and IM-2012 vs. ideal
967 mixing in S-2014 and VolatileCalc-Basalt; see Supporting Information Fig. S1).
968 As only 2 Low-Fo melt inclusions have vapor bubbles producing a FD ($N=2$), the
969 distribution of entrapment pressures calculated using just glass CO₂ contents are

970 indistinguishable from those using total CO₂ contents (dotted magenta vs. solid red
971 lines; Fig. 10a).

972 In contrast, there are substantial differences between the entrapment pressures
973 obtained from different solubility models for High-Fo melt inclusions (>Fo_{81.5}), with
974 MagmaSat and S-2014 plotting to significantly lower pressures than IM-2012 and
975 VolatileCalc-Basalt (both pairs are statistically indistinguishable from one another
976 at p=0.05; Fig. 10b). As discussed above, the simplification of the compositional
977 dependence in VolatileCalc-Basalt means that this model underestimates CO₂ solu-
978 bility, and therefore overestimates entrapment pressures for High-Fo melt inclusions
979 (Fig. 6c). Similarly, Iacono-Marziano et al. (2012) warn that their semi-empirical
980 model poorly incorporates the compositional effect of melt MgO contents on CO₂
981 solubility, as the vast majority of melts in their calibration dataset have ~6–8 wt%
982 MgO. In contrast, High-Fo PEC-corrected melt inclusions have MgO contents rang-
983 ing from 7.8–13.7 wt% (Fig. 6a). The calibration dataset for the S-2014 model
984 incorporates a significantly broader range of basaltic compositions, including melts
985 with MgO contents similar to PEC-corrected High-Fo melt inclusions (Fig. 6a). The
986 MagmaSat calibration dataset is similarly extensive (including the experiments used
987 to calibrate S-2014, IM-2012 and VolatileCalcBasalt). As for Low-Fo melt inclusions,
988 MagmaSat is offset to slightly lower pressures than S-2014 (median offset of 0.1
989 kbar).

990 Overall, we favour entrapment pressures from MagmaSat (Fig. 11, as it has
991 the largest calibration dataset, and is a full thermodynamic model (whereas S-2014
992 is purely empirical). Additionally, the S-2014 model predicts ~ 1 wt% H₂O at 0
993 bar, meaning that it is effectively evaluating the solubility of pure CO₂ for the H₂O
994 contents considered here (so shows no change in saturation pressure with variation
995 in H₂O contents between 0–1 wt% H₂O, see Supporting Information Fig. S1). As
996 shown in Fig. 10, differences between Shishkina and MagmaSat are relatively small.
997 For High-Fo inclusions, the differences between these models are statistically in-
998 significant, and easily overwhelmed with the errors associated with bubble volumes
999 (error bars on Fig. 11a). For completeness, Supporting Information Fig. S12 shows
1000 forsterite vs. depth plots similar to those shown in Fig. 11 for reconstructions using
1001 Shishkina, and for measured and fixed H₂O contents.

1002 Using MagmaSat, Low-Fo melt inclusions yield median entrapment depths
1003 (assuming $\rho=2400 \text{ kg/m}^{-3}$) of 1.44 km (lower and upper 68%=0.89–1.74 km). The
1004 median centroid depth, aspect ratio and reservoir volume derived from modelling of
1005 the first stage of the 2018 caldera collapse by Anderson et al. (2019) suggests that
1006 the HMM reservoir spans depths of 0.82–3.1 km, which aligns well with our entrap-
1007 ment depths, which mainly cluster in the top half of that range (perhaps suggesting
1008 melt inclusion formation was favoured in the upper half of the reservoir). The low
1009 PEC amounts experienced by these melt inclusions, the absence of cracks, and the
1010 fact that the two Low-Fo inclusions which did yield a diad had very low CO_2 den-
1011 sities (Fig. 4c), suggests that melt inclusions with a vapor bubble which did not
1012 produce a FD likely contained very small quantities of CO_2 (because the bubble
1013 predominantly forming during syn-eruptive quench; Fig. 9). Thus, we also consider
1014 entrapment depths from these melt inclusions (diamond shapes on Fig. 11a). This
1015 extends the distribution of entrapment depths to slightly deeper depths, which show
1016 an even better overlap with the depths of the HMM reservoir suggested by Anderson
1017 et al. (2019).

1018 Considering only High-Fo melt inclusions with a measurable Fermi diad (due to
1019 the uncertainty in the amount of CO_2 held within vapor bubbles which did not pro-
1020 duce a FD in melt inclusions which have undergone extensive PEC), the distribution
1021 of entrapment depths (KS test, $p=1.6 \times 10^{-7}$) and means (ANOVA, $p=2.5 \times 10^{-6}$) are
1022 offset to significantly higher pressures than Low-Fo melt inclusions (Fig. 11a). Con-
1023 sidering the error associated with reconstructing bubble CO_2 contents from bubble
1024 volumes estimated from 2D images (shown in pink on Fig. 10b), the distribution of
1025 entrapment depths for High-Fo olivines overlaps remarkably well with geophysical
1026 estimates of the depth of the SC reservoir (3–5 km; Poland et al., 2015). In detail,
1027 High-Fo olivines seem to form two main groups, one located at ~ 2 km depth, and a
1028 second located at 3–5 km depth (Fig. 11a).

1029 The quench-dominated mechanism of bubble growth in Low-Fo olivines means
1030 that very little CO_2 is held within the vapor bubble. Thus, entrapment depths
1031 calculated using glass-only measurements are statistically indistinguishable from
1032 those combining bubble and glass measurements (Fig. 10a). In contrast, entrapment
1033 depths calculated using just glass CO_2 contents in High-Fo olivines are anomalously
1034 shallow (median=0.38 km, lower and upper 68%=0.3–0.51 km; Fig. 11b), because

1035 bubble growth at high temperatures during PEC has resulted in the vast majority of
1036 the CO₂ entering the vapor bubble (Fig. 9).

1037 Use of EOS techniques to reconstruct CO₂ contents of vapor bubbles yields
1038 very high entrapment depths for Low-Fo olivines (median=3.3 km, lower and upper
1039 68%=0.89–10.8 km). Crucially, 13 inclusions yield entrapment depths >5 km (the
1040 inferred base of the SC reservoir), because the EOS method drastically overestimates
1041 bubble CO₂ densities in inclusions which have experienced minimal PEC (Fig. 8b-c).
1042 For High-Fo olivines, there is a better overlap between entrapment depths calculated
1043 using EOS methods, and Raman measurements, and EOS methods get closer to the
1044 true distribution of entrapment pressures than measurements of only the glass phase
1045 (Fig. 10b). However, EOS methods still predict that 23 melt inclusions crystallized
1046 at >5 km depth, with one forming at 26.4 km, compared to only two entrapment
1047 depths at 6.3 and 8.8 km using Raman reconstructions of bubble CO₂.

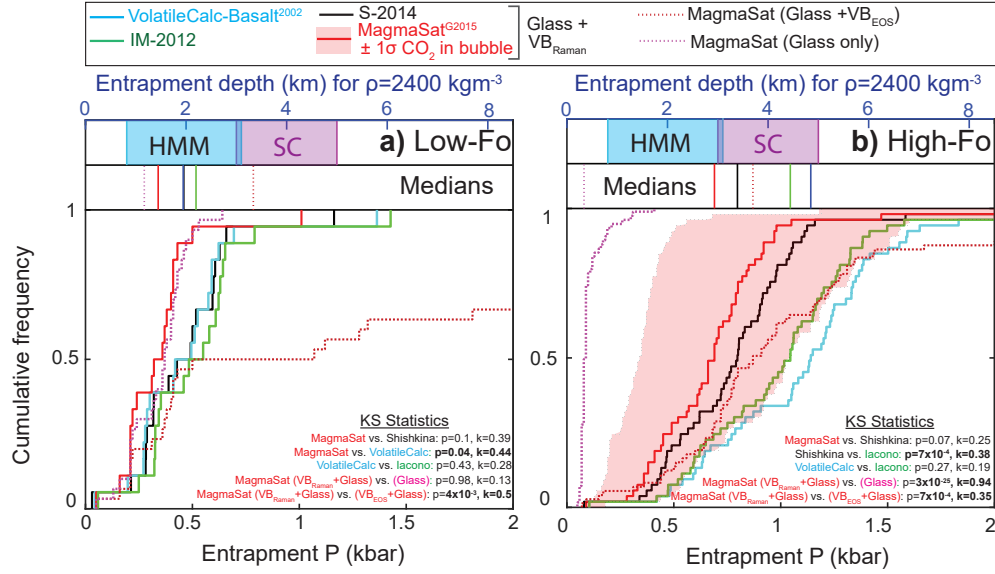


Figure 10. Cumulative distribution functions of entrapment pressures from different solubility models (major elements and CO_2 abundances corrected for the effects of PEC), with p values and test statistics from the KS test shown for different comparisons. a) Entrapment pressures for melt inclusion hosted in Low-Fo olivines (for melt inclusions with no VB, or a VB with a FD). Assuming $\rho=2400 \text{ kg/m}^3$, the median depths for all solubility models align well with the depth range of the HMM reservoir from modelling of the first stage of the 2018 caldera collapse by Anderson et al. (2019) (upper and lower limits calculated from their median volume, centroid depth, and aspect ratio; cyan bar). The distributions of entrapment pressures from MagmaSat calculated from total carbon contents (bubbles+glass; red line) vs. glass only measurements (pink dotted line) are statistically indistinguishable. Entrapment pressures from MagmaSat where bubble CO_2 contents are calculated using the EOS method lie to significantly higher pressures (deep red dotted line). b) Entrapment pressures calculated for melt inclusions hosted in High-Fo olivines (for melt inclusions with a VB producing a FD). The light red region shows the error on MagmaSat entrapment pressures resulting from uncertainty in estimating bubble proportions from 2D images (Tucker et al., 2019). This aligns well with geophysical estimates of the depth of the SC reservoir (3–5 km, magenta bar; Poland et al., 2015). Entrapment pressures from MagmaSat calculated using only glass CO_2 contents (dotted magenta line) are offset to very low pressures extremely low pressures. Entrapment pressures calculated from bubble reconstructed using the EOS method are also offset to anomalously high pressures. In a-b), all melt inclusions are shown for glass-only measurements and EOS calculations, because studies which do not perform Raman measurements cannot distinguish between bubbles with and without a FD.

5.6 Summit-Rift Connectivity

Melt inclusion entrapment depths indicate that olivine crystals erupted at F8 crystallized within both the shallower HMM reservoir (Low-Fo olivines) and the deeper, SC reservoir (High-Fo olivines). The low degrees of olivine-melt disequilibrium and limited amounts of PEC experienced by melt inclusions hosted within Low-Fo olivines implies that these crystals grew in a melt with a similar Mg#, and therefore temperature, to the carrier melt in which they were erupted. In contrast, the high degrees of olivine-melt disequilibrium and large amounts of PEC indicates that High-Fo crystals were mixed into a significantly lower Mg# (and therefore cooler) carrier liquid than the liquid in which they crystallized. Based on reports of lattice distortions (Gansecki et al., 2019) in some F8 olivines, high core forsterite contents, and the clustering of entrapment pressures between 3–5 km (Fig. 11), we suggest that these olivines grew in the SC reservoir, and then settled into mush piles at the base of this reservoir where they were stored for prolonged periods (perhaps as long as centuries to millenia; Wieser, Edmonds, et al., 2020).

Seismic swarms and the initiation of inflationary tilt in March to April 2018 have been interpreted to record the injection of new melts into the South Caldera reservoir (Neal et al., 2019; Flinders et al., 2020), which may have disturbed the olivine mush pile. These new melts (along with the High-Fo olivines they scavenged) would then have mixed into the cooler, lower Mg# melts present within the middle to upper parts of the SC reservoir. Alternatively, if inflationary signals were generated by a reduction in the amount of magma flowing along the ERZ to Pu‘u ‘Ō‘ō (Patrick et al., 2020), progressive internal pressurization of the SC reservoir could also disturb piles of settled crystals. Rapid cooling of mush-derived olivines following their mixing into more evolved melts would have initiated large amounts of PEC. Using the method of Danyushevsky et al. (2002, 2000), the degrees of Mg# re-equilibration between melt inclusions and host olivine crystals (~70-100%) indicate that crystals were resident in these cooler melts for timescales of approximately a month to a year prior to their eruption at Fissure 8. This is consistent with the time lag between geophysical signals indicating increasing pressurization of the magmatic system in March, and the eruption of crystals between late May and August.

1079 The fact that only two melt inclusions record entrapment depths >5 km rules
1080 out models where high forsterite olivines grew in deeper magma storage reservoirs
1081 near the base of the volcanic pile (as suggested for Kīlauea's prehistoric explosive
1082 period by Lynn et al., 2017), or within Kīlauea's deep rift zones at ~ 6 –9 km (Fig 11
1083 Clague & Denlinger, 1994).

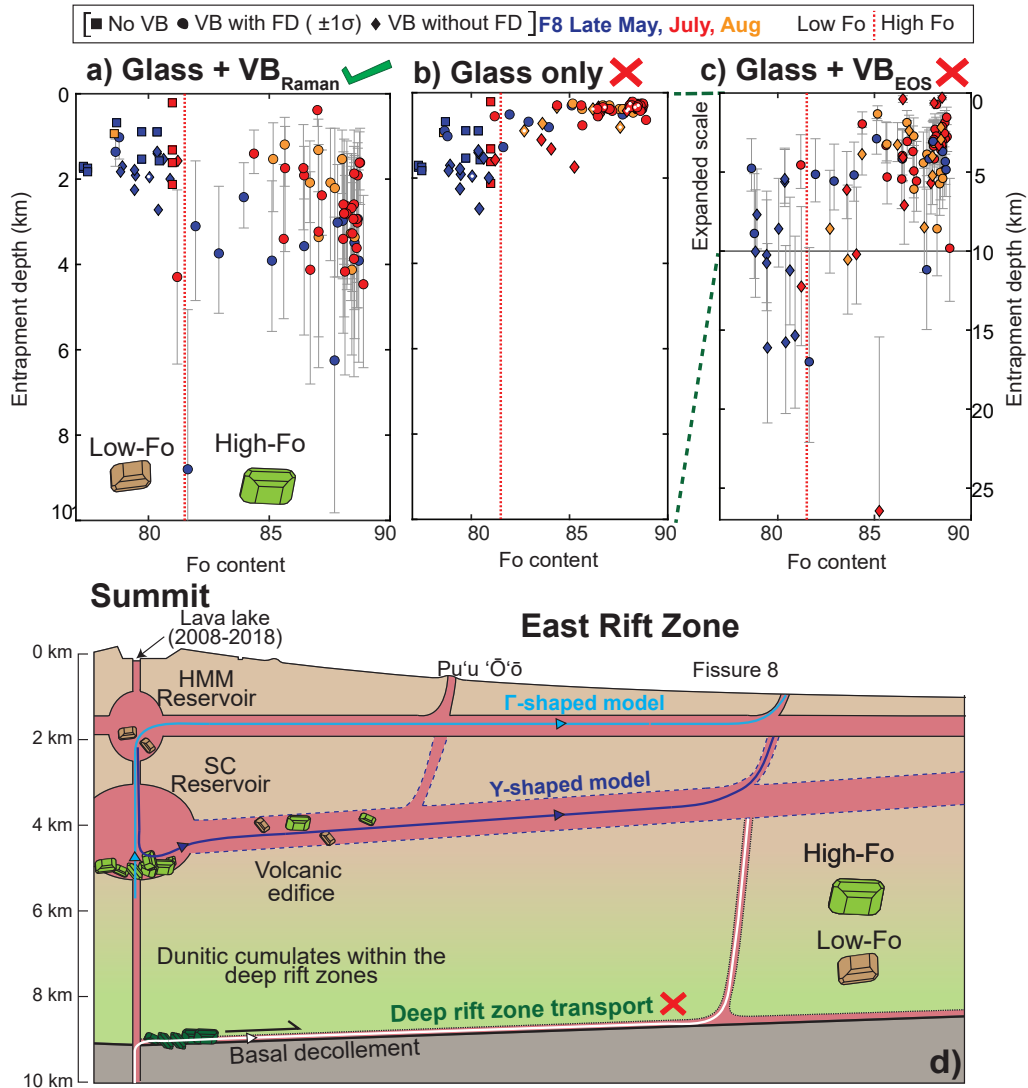


Figure 11.

1084 **Caption Fig. 11.** Schematic diagram of Kilauea's plumbing system, informed
 1085 by entrapment depths from MagmaSat for PEC-corrected melt inclusion compo-
 1086 sitions (assuming $\rho=2400 \text{ kg/m}^3$ following Anderson et al. (2019)). a) Preferred
 1087 entrapment depths from this study (all melt inclusions for Low-Fo olivines, only
 1088 those with a FD for High-Fo olivines). Error bars on bubble-free melt inclusions
 1089 from SIMS analyses are smaller than the symbol size. Error bars for bubble-bearing
 1090 melt inclusions were calculated from the minimum and maximum possible total CO_2
 1091 content using the 1σ error calculated from repeated Raman analyses of each bubble,
 1092 and the 1σ estimated by Tucker et al. (2019) associated with calculating 3D bubble

1093 volume proportions from 2D images (-48 to 37%). b) Entrapment depths estimated
1094 from analyses of only the glass phase are anomalously shallow for High-Fo olivines.
1095 c) Entrapment depths using the EOS method to reconstruct bubble CO₂ contents
1096 are anomalously deep, with large numbers of inclusions plotting at >5 km depth
1097 (note change in scale). Error bar reflects the uncertainty associated with calculating
1098 3D bubble volume proportions from 2D images. d) Cross section showing the three
1099 hypothesized magma transport paths supplying rift zone eruptions.

1100 The mechanism by which crystal populations grown in the HMM and SC
1101 reservoirs were mixed into a single carrier melt encapsulates an ongoing debate at
1102 Kīlauea regarding the geometry of the connection between the rift zone conduit and
1103 the summit reservoir system. This connection has been variably described as a Y-
1104 shaped feeder system with the SC reservoir feeding both the HMM reservoir and the
1105 ERZ conduit with two discrete conduits (Pietruszka et al., 2018; Poland et al., 2015,
1106 Model 2, Fig. 11d), or a Γ -shaped feeder system with a vertical conduit between the
1107 HMM and the SC reservoir, and a single, near-horizontal conduit from the HMM
1108 reservoir into the ERZ (Cervelli & Miklius, 2003, Model 3, Fig. 11d). Cervelli and
1109 Miklius (2003) suggest that the Γ -shaped model is more plausible because a shal-
1110 low conduit (which is subject to less lithostatic pressure) is more likely to remain
1111 open during pauses in eruptive activity than a deep conduit, and because shallow
1112 intrusions into the upper ERZ influence both the HMM reservoir and activity at
1113 Pu‘u ‘Ō‘ō. However, Poland et al. (2015) favour the Y-shaped model based on earth-
1114 quake and InSAR observations that dyke intrusions into the ERZ in 2007 and 2011
1115 ascended from a depth of \sim 2–3 km.

1116 For both reservoir geometries, the olivine mush pile at the base of the SC
1117 reservoir may have been disturbed by the input of new magma into Kīlauea’s sum-
1118 mit inferred from geophysical signals (Neal et al., 2019; Flinders et al., 2020), or
1119 progressive internal pressurization due to a drop in magma output to Pu‘u ‘Ō‘ō.
1120 In the Γ -shaped model, High-Fo crystals sourced from the SC mush pile may have
1121 ascended into the HMM reservoir, and then been transported along a shallow rift
1122 zone conduit to the site of the eruption along with Low-Fo olivines. However, the
1123 Y-shaped model provides an additional mechanism by which to disturb the SC mush
1124 pile. In this geometry, melts from the HMM reservoir carrying Low-Fo olivine crys-
1125 tals would have drained down through the SC reservoir before passing out onto

1126 the rift zone, with significant potential for this downward flow, aided by the large
1127 scale collapse of Kīlauea’s caldera, to erode the SC mush pile. Interestingly, the pro-
1128 portion of crystals which are out of equilibrium with their carrier melts increases
1129 substantially between May-August 2018 (Fig. 2a), and the degree of re-equilibration
1130 between melt inclusions and host crystals decreases (Fig. 3b).

1131 If the disturbance to the mush pile was solely the result of pressurization of
1132 the volcanic plumbing system, it might be expected that the majority of High-Fo
1133 olivines were disturbed from their mush piles in mid-March to April 2019, when in-
1134 flationary signals were the strongest (Patrick et al., 2020; Neal et al., 2019). In this
1135 scenario, High-Fo olivines might be expected to be more dominant in the May-18 vs.
1136 July and Aug-18 samples. In contrast, increasing erosion and scavenging of High-
1137 Fo olivines during the downdraining of melts from the HMM reservoir into the SC
1138 reservoir during the summit collapse could account for the increase in the proportion
1139 of High-Fo olivines with time, similar to the mechanism suggested by Teasdale et al.
1140 (2005) for the 1998 eruption of Cerro Azul, Galápagos. Erosion of the mush pile by
1141 down-draining from the shallower HMM reservoir, into which the summit caldera
1142 was collapsing, also accounts for the fact that High-Fo olivines were extremely rare
1143 during the 35 year Pu‘u ‘Ō‘ō eruption.

1144 Another possibility is that some melt inclusions were trapped during the 40
1145 km of transport down the ERZ to the site of the eruption (Patrick, Dietterich, et al.,
1146 2019). Assessing this hypothesis requires assumptions regarding the depth of magma
1147 transport. Given that the dyke to the LERZ propagated downrift from Pu‘u ‘Ō‘ō,
1148 we assume that the dyke had a similar depth to intrusions within the proximity of
1149 Pu‘u ‘Ō‘ō between 1997–2007, which have been studied in detail, and shown to rise
1150 from the ERZ conduit at depths of ~ 2 –2.4 km (Owen et al., 2000; Montgomery-
1151 Brown et al., 2011, and refs within). Thus, it is plausible that some of the Low-Fo
1152 olivines with entrapment depths near ~ 2 km may have growth in the rift zone. How-
1153 ever, crystallization within the ERZ conduit and dyke would likely occur throughout
1154 the eruption, yet the abundance of Low-Fo olivine crystals declines as the eruption
1155 proceeds

1156 The cluster of High-Fo olivines at ~ 2 km could also represent crystallization
1157 during down-rift transport. These olivine crystals have Fo contents between 84 and

1158 89, which must have grown from melts with MgO contents between 8.5–13.1 wt%
1159 (for $K_D=0.3$, $\text{FeO}_T=11.33$ wt%, with $\text{Fe}^{3+}/\text{Fe}_T=0.15$). Yet, the highest erupted
1160 glass MgO content during the 2018 LERZ eruption is 6.74 wt% MgO (Fig. 3a and
1161 Gansecki et al., 2019). Moreover, glass MgO contents during the 35-year Pu‘u ‘Ō‘ō
1162 eruption did not exceed 8 wt% MgO (see Fig. 8.2 Thornber et al., 2015), suggesting
1163 that high MgO melts may not have been present in the rift zone conduit since the
1164 early phases of the Mauna Ulu eruption in 1969 (Wieser et al., 2019). In contrast,
1165 based on the occurrence of high MgO glass shards in a number of eruptions around
1166 the summit caldera, Helz et al. (2015) suggest that melts with 6.5–11 wt% MgO are
1167 present in the summit reservoir over many centuries. This supports our inference
1168 that the High-Fo olivines erupted at F8 crystallized from high MgO melts supplied
1169 from the Hawaiian mantle plume within the SC reservoir. These high MgO melts are
1170 very rarely erupted at the surface as they rapidly mix with more evolved, resident
1171 melts within the reservoir, so the only record of their existence are the olivines they
1172 crystallize. Given the rarity of these high MgO melts at the surface, it is difficult to
1173 imagine a situation where these melts would avoid mixing with resident magmas in
1174 the summit reservoir, and manage to ascend prolonged distances along the ERZ con-
1175 duct (which must be dominated by low MgO melts based on the composition of the
1176 co-erupted carrier liquid at F8). Finally, if these High-Fo olivines crystallized in the
1177 rift zone, they must have been resident for between a month and a year before they
1178 erupted at F8 (based on the degree of Mg# re-equilibration between melt inclusions
1179 and host olivine crystals).

1180 Interestingly, the May-18 sample does not show the distinctive clustering of
1181 High-Fo entrapment depths at ~ 2 km seen in the July and Aug-18 sample. This
1182 may result from the relatively small number of measurements of High-Fo olivines
1183 in this sample ($N=12$). Alternatively, it may suggest that the two reservoirs be-
1184 came increasingly connected during the collapse of the summit caldera, allowing
1185 remobilized High-Fo crystals from the SC mush pile to be transported up into the
1186 shallower HMM reservoir. The juxtaposition of these hot crystals with cooler melts
1187 within this reservoir may have led to dissolution or rapid growth (Shea et al., 2019;
1188 Mourey et al., 2020), favouring the formation of embayments. Perhaps due to the
1189 mixing with a hotter, and higher Mg# melt, growth may have resumed, sealing off
1190 melt inclusions recording shallower entrapment depths, before the crystal cargo was

1191 drained back down in the SC reservoir, and out along the ERZ conduit. It is also
1192 possible that the two reservoir systems always have a higher degree of connectivity
1193 than indicated by schematic diagrams such as Fig. 11, with frequent cycling of melt
1194 and crystals between the two reservoirs (and it is simply chance that these lower P
1195 inclusions were not seen in the May-18 sample). Further investigation of geophysical
1196 datasets from the 2018 eruption should provide tighter constraints on the depth of
1197 rift zone transport and dike propagation, allowing more rigorous assessments of the
1198 magma transport geometries indicated by our barometric estimates. Additionally,
1199 more detailed work on timescales from diffusive re-equilibration of Fe-Mg in both
1200 melt inclusions and host crystals will help evaluate differences between the High-Fo
1201 crystal cargo erupted at F8 between May and August.

1202 **6 Conclusion**

1203 Detailed investigations of melt inclusion volatile systematics from the 2018
1204 eruption of Kīlauea reveal that the erupted crystal cargo originated from both the
1205 Halema'uma'u reservoir (Low-Fo olivines; $\sim 1\text{--}2$ km depth) and the South Caldera
1206 reservoir (High-Fo olivines, $\sim 3\text{--}5$ km depth). This demonstrates that in addition to
1207 the supply of magma from the HMM reservoir inferred from geophysical modelling
1208 of the summit collapse (Anderson et al., 2019), a substantial volume of magma must
1209 also have been derived from the SC reservoir in order to transport these High-Fo
1210 crystals to the surface. This supports recent estimates of the total amount of SO_2
1211 emitted from F8 (Kern et al., 2020), which requires the erupted volume to have
1212 been approximately twice that inferred to have drained from the HMM reservoir by
1213 Anderson et al. (2019).

1214 High-Fo Melt inclusions, which mostly yield entrapment depths aligned with
1215 geophysical estimates of the depth of the SC reservoir ($\sim 3\text{--}5$ km), host the vast
1216 majority of their CO_2 budget in the vapor bubble ($\sim 90\%$). This is a consequence
1217 of the large amounts of PEC experienced by these melt inclusions following their
1218 entrainment into cooler, lower Mg# melts. Based on the textural and chemical
1219 similarities of these High-Fo crystals and those observed at previous eruptions at
1220 Kīlauea (Wieser, Edmonds, et al., 2020; Wieser et al., 2019), we suggest that these
1221 olivines grew from high MgO melts present at the base of the SC reservoir (Helz
1222 et al., 2015), and settled into mush piles for prolonged time periods. Based on the

1223 degree of Mg# re-equilibration between melt inclusions and host olivines, we sug-
1224 gest that these olivines were mobilized from mush piles and mixed into lower Mg#
1225 carrier melts approximately a month to a year before they erupted at Fissure 8.
1226 This disturbance may correspond with the onset of geophysical signals of inflation
1227 in March-April, 2018, interpreted to represent the injection of new melts into the
1228 plumbing system, or a reduction in output from the summit reservoir (Flinders et
1229 al., 2020; Patrick et al., 2020). Because of the large amount of CO₂ in the vapour
1230 bubbles of these inclusions, entrapment depths calculated using only glass CO₂ con-
1231 tents would yield anomalously low entrapment depths (~0.3–0.5 km), and fail to
1232 recognise that the SC reservoir supplied significant volumes of magma to Fissure 8.

1233 In contrast, Low-Fo melt inclusions are closer to equilibrium with their carrier
1234 melts, so have experienced smaller amounts of PEC. Where present, the vapor bub-
1235 ble in these melt inclusions is very CO₂-poor, and grew most of its volume during
1236 during syn-eruptive quenching (~90%). As the quench rates of these samples mean
1237 that there was almost no diffusion of CO₂ between the melt and bubble during this
1238 growth phase, reconstructions of bubble CO₂ using equation of state methods yield
1239 anomalously high entrapment depths (4.5–16.1 km; Fig. 11c).

1240 Careful choice of a CO₂-H₂O solubility model is also vital to obtain accurate
1241 entrapment pressures, and therefore depths. Importantly, the basaltic functions of
1242 VolatileCalc, which has been used the majority of previous Kīlauean melt inclusion
1243 studies, overpredict entrapment pressures for High-Fo melt inclusions, due to the
1244 simplified relationship between CO₂ solubility and melt composition in this model.
1245 Like EOS methods, use of this model would indicate that ~50% of melt inclusions
1246 crystallized deeper than the base of the SC reservoir at >5 km (requiring the pres-
1247 ence of a previously unrecognised storage reservoir; Fig. 10).

1248 Overall, our study highlights the importance of measuring bubble densities using
1249 Raman Spectroscopy in addition to measurements of the melt phase by SIMS or
1250 FTIR. We also emphasize the importance of carefully evaluating the compositional
1251 range of different solubility models relative to the melt composition of interest. The
1252 strong agreement between our entrapment depths and models of magma storage
1253 inferred from geophysical datasets at Kīlauea shows that melt inclusion records are

1254 a powerful tool to accurately constrain the location of magma storage reservoirs
1255 supplying volcanic eruptions.

1256 **Acknowledgments**

1257 This work was funded through a NERC DTP studentship to PW (NE/L002507/1),
1258 a NERC ion microprobe grant (IMF675/1118), two Cambridge University Leave to
1259 Work away grants, and a grant from the NERC Centre for Observation and Mod-
1260 elling of Earthquakes, Volcanoes and Tectonics (COMET). We thank Iris Buisman
1261 for help collecting EPMA data, Cees-Jan de Hoog and John Craven at the Edin-
1262 burgh Ion Microprobe Facility for their assistance collecting SIMS data, and Richard
1263 Taylor (Zeiss) for collecting the EDS maps shown in the Supporting Information.
1264 We thank Emily Mason, Emma Liu, and Dave Schneider for help collecting samples
1265 in the field. We are very grateful to Jonathon Tucker to helping us to reproduce the
1266 EOS calculations in his paper, and for helpful discussions about bubble walls. Fi-
1267 nally, we thank Paul Wallace, Kendra Lynn and one anonymous reviewer, along with
1268 the editor Ken Rubin for their helpful comments that greatly improved the quality
1269 of this manuscript.

1270 **Data Availability** The melt inclusion and glass compositions presented in
1271 this paper are provided as an excel spreadsheet. This data has been uploaded to
1272 the Cambridge University Repository <https://doi.org/10.17863/CAM.60202>, and
1273 is also available on Github <https://github.com/PennyWieser/G3-2018-MI>. This
1274 spreadsheet also contains the results of the bubble growth models shown in Fig. 9.

1275 **References**

- 1276 Anderson. (1974). Evidence for a picritic, volatile-rich magma beneath Mt. Shasta,
1277 California. *Journal of Petrology*, 15(2), 243–267.
- 1278 Anderson, & Brown, G. G. (1993). CO₂ contents and formation pressures of some
1279 Kilauean melt inclusions. *American Mineralogist*, 78(7-8), 794–803.
- 1280 Anderson, Johanson, I. A., Patrick, M., Gu, M., Segall, P., Poland, M. P., ... Mik-
1281 lius, A. (2019). Magma reservoir failure and the onset of caldera collapse at
1282 kilauea volcano in 2018. *Science*, 366(6470).
- 1283 Antoshechkina, P. M., & Ghiorso, M. S. (2018). MELTS for MATLAB: A new edu-
1284 cational and research tool for computational thermodynamics. *AGUFM*, 2018,

- 1285 ED44B-23.
- 1286 Aster, E. M., Wallace, P. J., Moore, L. R., Watkins, J., Gazel, E., & Bodnar, R. J.
1287 (2016). Reconstructing CO₂ concentrations in basaltic melt inclusions using
1288 raman analysis of vapor bubbles. *Journal of Volcanology and Geothermal*
1289 *Research*, 323, 148–162.
- 1290 Baker, S., & Amelung, F. (2012). Top-down inflation and deflation at the summit of
1291 kīlauea volcano, hawaii ‘i observed with insar. *Journal of Geophysical Research:*
1292 *Solid Earth*, 117(B12).
- 1293 Barth, A., Newcombe, M., Plank, T., Gonnermann, H., Hajimirza, S., Soto, G. J.,
1294 ... Hauri, E. (2019). Magma decompression rate correlates with explosivity
1295 at basaltic volcanoes—constraints from water diffusion in olivine. *Journal of*
1296 *Volcanology and Geothermal Research*, 387, 106664.
- 1297 Bell, I. H., Wronski, J., Quoilin, S., & Lemort, V. (2014). Pure and pseudo-pure
1298 fluid thermophysical property evaluation and the open-source thermophysical
1299 property library coolprop. *Industrial & engineering chemistry research*, 53(6),
1300 2498–2508.
- 1301 Bennett, E. N., Jenner, F. E., Millet, M.-A., Cashman, K. V., & Lissenberg, C. J.
1302 (2019). Deep roots for mid-ocean-ridge volcanoes revealed by plagioclase-
1303 hosted melt inclusions. *Nature*, 572(7768), 235–239.
- 1304 Cervelli, P. F., & Miklius, A. (2003). The shallow magmatic system of kilauea vol-
1305 cano. *US Geological Survey Professional Paper*, 1676, 149–163.
- 1306 Chakraborty, S. (2010). Diffusion coefficients in olivine, wadsleyite and ringwoodite.
1307 *Reviews in mineralogy and geochemistry*, 72(1), 603–639.
- 1308 Clague, D., & Denlinger, R. (1994). Role of olivine cumulates in destabilizing the
1309 flanks of hawaiian volcanoes. *Bulletin of Volcanology*, 56(6-7), 425–434.
- 1310 Clague, D., Moore, J., Dixon, J., & Friesen, W. (1995). Petrology of submarine lavas
1311 from kilauea’s puna ridge, hawaii. *Journal of Petrology*, 36(2), 299–349.
- 1312 Collins, S., MacLennan, J., Pyle, D., Barnes, S.-J., & Upton, B. (2012). Two phases
1313 of sulphide saturation in réunion magmas: Evidence from cumulates. *Earth*
1314 *and Planetary Science Letters*, 337, 104–113.
- 1315 Danyushevsky, L., Della-Pasqua, F., & Sokolov, S. (2000). Re-equilibration of melt
1316 inclusions trapped by magnesian olivine phenocrysts from subduction-related
1317 magmas: petrological implications. *Contributions to Mineralogy and Petrology*,

- 1318 138(1), 68–83.
- 1319 Danyushevsky, L., & Plechov, P. (2011). Petrolog3: Integrated software for modeling
1320 crystallization processes. *Geochemistry, Geophysics, Geosystems*, 12(7).
- 1321 Danyushevsky, L., Sokolov, S., & Falloon, T. J. (2002). Melt inclusions in olivine
1322 phenocrysts: using diffusive re-equilibration to determine the cooling history
1323 of a crystal, with implications for the origin of olivine-phyric volcanic rocks.
1324 *Journal of Petrology*, 43(9), 1651–1671.
- 1325 Dixon, J. E. (1997). Degassing of alkalic basalts. *American Mineralogist*, 82(3-4),
1326 368–378.
- 1327 Dixon, J. E., Clague, D. A., & Stolper, E. M. (1991). Degassing history of water,
1328 sulfur, and carbon in submarine lavas from kilauea volcano, hawaii. *The Jour-
1329 nal of Geology*, 99(3), 371–394.
- 1330 Dixon, J. E., Clague, D. A., Wallace, P., & Poreda, R. (1997). Volatiles in alkalic
1331 basalts form the north arch volcanic field, hawaii: extensive degassing of deep
1332 submarine-erupted alkalic series lavas. *Journal of Petrology*, 38(7), 911–939.
- 1333 Dixon, J. E., Stolper, E. M., & Holloway, J. R. (1995). An experimental study of
1334 water and carbon dioxide solubilities in mid-ocean ridge basaltic liquids. part i:
1335 calibration and solubility models. *Journal of Petrology*, 36(6), 1607–1631.
- 1336 Duan, Z., & Zhang, Z. (2006). Equation of state of the h₂o, co₂, and h₂o–co₂ sys-
1337 tems up to 10 gpa and 2573.15 k: Molecular dynamics simulations with ab
1338 initio potential surface. *Geochimica et cosmochimica acta*, 70(9), 2311–2324.
- 1339 Eaton, J. P., & Murata, K. (1960). How volcanoes grow. *Science*, 132(3432), 925–
1340 938.
- 1341 Esposito, R., Bodnar, R., Danyushevsky, L., De Vivo, B., Fedele, L., Hunter, J.,
1342 ... Shimizu, N. (2011). Volatile evolution of magma associated with the
1343 solchiaro eruption in the phlegrean volcanic district (italy). *Journal of Petrol-
1344 ogy*, 52(12), 2431–2460.
- 1345 Esposito, R., Klebesz, R., Bartoli, O., Klyukin, Y., Moncada, D., Doherty, A., &
1346 Bodnar, R. (2012). Application of the linkam ts1400xy heating stage to melt
1347 inclusion studies. *Open Geosciences*, 4(2), 208–218.
- 1348 Fermi, E. (1931). Über den ramaneffekt des kohlendioxyds. *Zeitschrift für Physik*,
1349 71, 250-259.
- 1350 Fiske, R. S., & Kinoshita, W. T. (1969). Inflation of kilauea volcano prior to its

- 1351 1967-1968 eruption. *Science*, *165*(3891), 341–349.
- 1352 Flinders, A., Caudron, C., Johanson, I., Taira, T., Shiro, B., & Haney, M. (2020).
1353 Seismic velocity variations associated with the 2018 lower east rift zone erup-
1354 tion of kīlauea, hawaii. *Bulletin of Volcanology*, *82*, 47.
- 1355 Gaetani, G. A., O’Leary, J. A., Shimizu, N., Bucholz, C. E., & Newville, M. (2012).
1356 Rapid reequilibration of h₂o and oxygen fugacity in olivine-hosted melt inclu-
1357 sions. *Geology*, *40*(10), 915–918.
- 1358 Gansecki, C., Lee, R. L., Shea, T., Lundblad, S. P., Hon, K., & Parcheta, C. (2019).
1359 The tangled tale of kīlauea’s 2018 eruption as told by geochemical monitoring.
1360 *Science*, *366*(6470).
- 1361 Gerlach, T., McGee, K., Elias, T., Sutton, A., & Doukas, M. (2002). Carbon diox-
1362 ide emission rate of kīlauea volcano: Implications for primary magma and the
1363 summit reservoir. *Journal of Geophysical Research: Solid Earth*, *107*(B9),
1364 ECV–3.
- 1365 Ghiorso, M. S., & Gualda, G. A. (2015). An h₂o–co₂ mixed fluid saturation model
1366 compatible with rhyolite-melts. *Contributions to Mineralogy and Petrology*,
1367 *169*(6), 1–30.
- 1368 Giordano, D., Nichols, A. R., & Dingwell, D. B. (2005). Glass transition tem-
1369 peratures of natural hydrous melts: a relationship with shear viscosity and
1370 implications for the welding process. *Journal of Volcanology and Geothermal
1371 Research*, *142*(1-2), 105–118.
- 1372 Hartley, M. E., MacLennan, J., Edmonds, M., & Thordarson, T. (2014). Reconstruct-
1373 ing the deep co₂ degassing behaviour of large basaltic fissure eruptions. *Earth
1374 and Planetary Science Letters*, *393*, 120–131.
- 1375 Hartley, M. E., Neave, D. A., MacLennan, J., Edmonds, M., & Thordarson, T.
1376 (2015). Diffusive over-hydration of olivine-hosted melt inclusions. *Earth
1377 and Planetary Science Letters*, *425*, 168–178.
- 1378 Hauri, E. (2002). Sims analysis of volatiles in silicate glasses, 2: isotopes and abun-
1379 dances in hawaiian melt inclusions. *Chemical Geology*, *183*(1-4), 115–141.
- 1380 Helo, C., Longpré, M.-A., Shimizu, N., Clague, D. A., & Stix, J. (2011). Explosive
1381 eruptions at mid-ocean ridges driven by co₂-rich magmas. *Nature Geoscience*,
1382 *4*(4), 260–263.
- 1383 Helz, R., Clague, D., Mastin, L. G., & Rose, T. R. (2015). Evidence for large com-

- 1384 positional ranges in coeval melts erupted from kilauea’s summit reservoir.
 1385 *Hawaiian Volcanoes: from Source to Surface*, 125–145.
- 1386 Helz, R., Clague, D. A., Sisson, T. W., & Thornber, C. R. (2014). Petrologic insights
 1387 into basaltic volcanism at historically active hawaiian volcanoes. *US Geological*
 1388 *Survey Professional Paper, 1801*, 237–292.
- 1389 Helz, R., Cottrell, E., Brounce, M. N., & Kelley, K. A. (2017). Olivine-melt relation-
 1390 ships and syneruptive redox variations in the 1959 eruption of kilauea volcano
 1391 as revealed by xanes. *Journal of Volcanology and Geothermal Research, 333*,
 1392 1–14.
- 1393 Helz, R., & Thornber, C. R. (1987). Geothermometry of kilauea iki lava lake, hawaii.
 1394 *Bulletin of Volcanology, 49*(5), 651–668.
- 1395 Iacono-Marziano, G., Morizet, Y., Le Trong, E., & Gaillard, F. (2012). New experi-
 1396 mental data and semi-empirical parameterization of h₂o–co₂ solubility in mafic
 1397 melts. *Geochimica et Cosmochimica Acta, 97*, 1–23.
- 1398 Iacovino, K., Matthews, S., Wieser, P. E., Moore, G. M., & Begue, F. (2020). *Vesi-*
 1399 *cal v. 0.1.1*. Zenodo. Retrieved from <https://zenodo.org/record/4096463>
 1400 doi: 10.5281/ZENODO.4096463
- 1401 Iacovino, K., & Till, C. B. (2019). Densityx: A program for calculating the densities
 1402 of magmatic liquids up to 1,627 c and 30 kbar. *Volcanica, 2*(1), 1–10.
- 1403 Jarosewich, E. (2002). Smithsonian microbeam standards. *Journal of Research of the*
 1404 *National Institute of Standards and Technology, 107*(6), 681.
- 1405 Kauahikaua, J. P., & Trusdell, F. A. (2020). *Have humans influenced volcanic activ-*
 1406 *ity on the lower east rift zone of kilauea volcano? a publication review* (Tech.
 1407 Rep.). HVO: US Geological Survey.
- 1408 Kawakami, Y., Yamamoto, J., & Kagi, H. (2003). Micro-raman densimeter for
 1409 co₂ inclusions in mantle-derived minerals. *Applied spectroscopy, 57*(11), 1333–
 1410 1339.
- 1411 Kern, C., Lerner, A. H., Elias, T., Nadeau, P. A., Holland, L., Kelly, P. J., ... Cap-
 1412 pos, M. (2020). Quantifying gas emissions associated with the 2018 rift
 1413 eruption of kilauea volcano using ground-based doas measurements. *Bulletin of*
 1414 *Volcanology, 82*(7), 1–24.
- 1415 Lamadrid, H., Moore, L., Moncada, D., Rimstidt, J., Burruss, R., & Bodnar, R.
 1416 (2017). Reassessment of the raman co₂ densimeter. *Chemical Geology, 450*,

- 1417 210–222.
- 1418 Lee, R. L., Wagoner, L., Conrey, R., Gansecki, C., & Lundblad, S. (2019). *Whole-*
 1419 *rock chemical analyses of lava samples collected during the 2018 lower east*
 1420 *rift zone eruption of kilauea*. U.S. Geological Survey. Retrieved from
 1421 <https://www.sciencebase.gov/catalog/item/5d3279d2e4b01d82ce8791b2>
 1422 doi: 10.5066/P9LVY7GV
- 1423 Le Voyer, M., Asimow, P. D., Mosenfelder, J. L., Guan, Y., Wallace, P. J., Schiano,
 1424 P., ... Eiler, J. M. (2014). Zonation of h₂o and f concentrations around melt
 1425 inclusions in olivines. *Journal of Petrology*, *55*(4), 685–707.
- 1426 Lynn, K. J., Garcia, M., Shea, T., Costa, F., & Swanson, D. A. (2017). Timescales
 1427 of mixing and storage for keanakāko ‘i tephra magmas (1500–1820 ce), kīlauea
 1428 volcano, hawai ‘i. *Contributions to Mineralogy and Petrology*, *172*(9), 76.
- 1429 Maaløe, S., Pedersen, R. B., & James, D. (1988). Delayed fractionation of basaltic
 1430 lavas. *Contributions to Mineralogy and Petrology*, *98*(4), 401–407.
- 1431 Maclellan, J. (2017). Bubble formation and decrepitation control the co₂ content of
 1432 olivine-hosted melt inclusions. *Geochemistry, Geophysics, Geosystems*, *18*(2),
 1433 597–616.
- 1434 Matzen, A. K., Baker, M. B., Beckett, J. R., & Stolper, E. M. (2011). Fe–mg parti-
 1435 tioning between olivine and high-magnesian melts and the nature of hawaiian
 1436 parental liquids. *Journal of Petrology*, *52*(7-8), 1243–1263.
- 1437 Montgomery-Brown, E. K., Sinnett, D., Larson, K., Poland, M. P., Segall, P., &
 1438 Miklius, A. (2011). Spatiotemporal evolution of dike opening and décollement
 1439 slip at kīlauea volcano, hawai‘i. *Journal of Geophysical Research: Solid Earth*,
 1440 *116*(B3).
- 1441 Moore, L. R., Gazel, E., Tuohy, R., Lloyd, A. S., Esposito, R., Steele-MacInnis, M.,
 1442 ... Bodnar, R. J. (2015). Bubbles matter: An assessment of the contribution
 1443 of vapor bubbles to melt inclusion volatile budgets. *American Mineralogist*,
 1444 *100*(4), 806–823.
- 1445 Moore, L. R., Mironov, N., Portnyagin, M., Gazel, E., & Bodnar, R. J. (2018).
 1446 Volatile contents of primitive bubble-bearing melt inclusions from klyuchevskoy
 1447 volcano, kamchatka: Comparison of volatile contents determined by mass-
 1448 balance versus experimental homogenization. *Journal of Volcanology and*
 1449 *Geothermal Research*, *358*, 124–131.

- 1450 Mourey, A., Shea, T., Costa, F., Shiro, B., Oalman, J., Lee, L., & Gansecki,
 1451 C. (2020, August). Chalcophile elements track the fate of sulfur at
 1452 kīlauea volcano, hawai'i. *Goldschmidt Abstracts, 1858*, 1. Retrieved from
 1453 <https://goldschmidt.info/2020/abstracts/abstractView?id=2020003748>
 1454 doi: <https://goldschmidt.info/2020/abstracts/abstractView?id=2020003748>
- 1455 Moussallam, Y., Edmonds, M., Scaillet, B., Peters, N., Gennaro, E., Sides, I., &
 1456 Oppenheimer, C. (2016). The impact of degassing on the oxidation state of
 1457 basaltic magmas: a case study of kīlauea volcano. *Earth and Planetary Science*
 1458 *Letters, 450*, 317–325.
- 1459 Moussallam, Y., Oppenheimer, C., Scaillet, B., Gaillard, F., Kyle, P., Peters, N., ...
 1460 Donovan, A. (2014). Tracking the changing oxidation state of erebus magmas,
 1461 from mantle to surface, driven by magma ascent and degassing. *Earth and*
 1462 *Planetary Science Letters, 393*, 200–209.
- 1463 Neal, C., Brantley, S., Antolik, L., Babb, J., Burgess, M., Calles, K., ... others
 1464 (2019). The 2018 rift eruption and summit collapse of kīlauea volcano. *Sci-*
 1465 *ence, 363*(6425), 367–374.
- 1466 Neave, D. A., Hartley, M. E., MacLennan, J., Edmonds, M., & Thordarson, T.
 1467 (2017). Volatile and light lithophile elements in high-anorthite plagioclase-
 1468 hosted melt inclusions from iceland. *Geochimica et Cosmochimica Acta, 205*,
 1469 100–118.
- 1470 Neave, D. A., MacLennan, J., Hartley, M. E., Edmonds, M., & Thordarson, T.
 1471 (2014). Crystal storage and transfer in basaltic systems: the skuggafjöll erup-
 1472 tion, iceland. *Journal of Petrology, 55*(12), 2311–2346.
- 1473 Newman, S., & Lowenstern, J. B. (2002). Volatilecalc: a silicate melt–h₂O–CO₂ solu-
 1474 tion model written in visual basic for excel. *Computers & Geosciences, 28*(5),
 1475 597–604.
- 1476 Owen, S., Segall, P., Lisowski, M., Miklius, A., Murray, M., Bevis, M., & Foster, J.
 1477 (2000). January 30, 1997 eruptive event on kilauea volcano, hawaii, as moni-
 1478 tored by continuous gps. *Geophysical Research Letters, 27*(17), 2757–2760.
- 1479 Pamukcu, A. S., Gualda, G. A., & Rivers, M. L. (2013). Quantitative 3d pet-
 1480 rography using x-ray tomography 4: Assessing glass inclusion textures with
 1481 propagation phase-contrast tomography. *Geosphere, 9*(6), 1704–1713.
- 1482 Patrick, M., Dietterich, H., Lyons, J., Diefenbach, A., Parcheta, C., Anderson, ...

- 1483 Kauahikaua, J. (2019). Cyclic lava effusion during the 2018 eruption of kilauea
1484 volcano. *Science*, *366*(6470).
- 1485 Patrick, M., Houghton, B., Anderson, K., Poland, M., Montgomery-Brown, E., Jo-
1486 hanson, I., . . . Elias, T. (2020). The cascading origin of the 2018 kilauea
1487 eruption and implications for future forecasting. *Nature Communications*.
- 1488 Patrick, M., Orr, T., Anderson, & Swanson, D. (2019). Eruptions in sync: Im-
1489 proved constraints on kilauea volcano's hydraulic connection. *Earth and Plane-
1490 tary Science Letters*, *507*, 50–61.
- 1491 Pietruszka, A. J., Marske, J. P., Heaton, D. E., Garcia, M. O., & Rhodes, J. M.
1492 (2018). An isotopic perspective into the magmatic evolution and architecture
1493 of the rift zones of kilauea volcano. *Journal of Petrology*, *59*(12), 2311–2352.
- 1494 Poland, M. P., Miklius, A., & Montgomery-Brown, E. K. (2015). Magma supply,
1495 storage, and transport at shield-stage hawaiian volcanoes. *US Geological Sur-
1496 vey Professional Paper, 1801*, 179–234.
- 1497 Rasmussen, D., Plank, T., Wallace, P., Newcombe, M., & Lowenstern, J. (2020).
1498 Vapor-bubble growth in olivine-hosted melt inclusions. *American Mineralogist*.
1499 <https://doi.org/10.2138/am-2020-7377>.
- 1500 Riker, J. (2005). *The 1859 eruption of mauna loa volcano, hawai'i: Controls on the
1501 development of long lava channels* (Unpublished doctoral dissertation). Univer-
1502 sity of Oregon.
- 1503 Roedder, E. (1979). Origin and significance of magmatic inclusions. *Bulletin de Min-
1504 eralogie*, *102*(5), 487–510.
- 1505 Roedder, E. (1984). Fluid inclusions. *Reviews in mineralogy: Mineralogical Society
1506 of American*, v. 12.
- 1507 Roeder, P., & Emslie, R. (1970). Olivine-liquid equilibrium. *Contributions to Miner-
1508 alogy and Petrology*, *29*(4), 275–289.
- 1509 Rosso, K., & Bodnar, R. (1995). Microthermometric and raman spectroscopic
1510 detection limits of CO₂ in fluid inclusions and the raman spectroscopic charac-
1511 terization of CO₂. *Geochimica et Cosmochimica Acta*, *59*(19), 3961–3975.
- 1512 Ruth, D. C., Costa, F., de Maisonneuve, C. B., Franco, L., Cortés, J. A., & Calder,
1513 E. S. (2018). Crystal and melt inclusion timescales reveal the evolution of
1514 magma migration before eruption. *Nature Communications*, *9*(1), 2657.
- 1515 Ryan, M. P., & Sammis, C. G. (1981). The glass transition in basalt. *Journal of*

- 1516 *Geophysical Research: Solid Earth*, 86(B10), 9519–9535.
- 1517 Schneider, C. A., Rasband, W. S., & Eliceiri, K. W. (2012). Nih image to imagej: 25
1518 years of image analysis. *Nature methods*, 9(7), 671–675.
- 1519 Shea, T., Hammer, J. E., Hellebrand, E., Mourey, A. J., Costa, F., First, E. C., . . .
1520 Melnik, O. (2019). Phosphorus and aluminum zoning in olivine: contrast-
1521 ing behavior of two nominally incompatible trace elements. *Contributions to*
1522 *Mineralogy and Petrology*, 174(10), 85.
- 1523 Shishkina, T., Botcharnikov, R., Holtz, F., Almeev, R., & Portnyagin, M. V. (2010).
1524 Solubility of h₂O- and CO₂-bearing fluids in tholeiitic basalts at pressures up to
1525 500 mpa. *Chemical geology*, 277(1-2), 115–125.
- 1526 Shishkina, T., Botcharnikov, R. E., Holtz, F., Almeev, R. R., Jazwa, A. M., & Jaku-
1527 biak, A. A. (2014). Compositional and pressure effects on the solubility of h₂O
1528 and CO₂ in mafic melts. *Chemical Geology*, 388, 112–129.
- 1529 Sides, I., Edmonds, M., MacLennan, J., Houghton, B. F., Swanson, D., & Steele-
1530 MacInnis, M. J. (2014). Magma mixing and high fountaining during the
1531 1959 kīlauea Iki eruption, Hawai‘i. *Earth and Planetary Science Letters*, 400,
1532 102–112.
- 1533 Sides, I., Edmonds, M., MacLennan, J., Swanson, D., & Houghton, B. (2014). Erup-
1534 tion style at kīlauea volcano in Hawai‘i linked to primary melt composition.
1535 *Nature Geoscience*, 7(6), 464–469.
- 1536 Skirius, C. M., Peterson, J. W., & Anderson. (1990). Homogenizing rhyolitic glass
1537 inclusions from the Bishop tuff. *American Mineralogist*, 75(11-12), 1381–1398.
- 1538 Span, R., & Wagner, W. (1996). A new equation of state for carbon dioxide covering
1539 the fluid region from the triple-point temperature to 1100 K at pressures up to
1540 800 mpa. *Journal of physical and chemical reference data*, 25(6), 1509–1596.
- 1541 Steele-Macinnis, M., Esposito, R., & Bodnar, R. J. (2011). Thermodynamic model
1542 for the effect of post-entrapment crystallization on the h₂O–CO₂ systematics
1543 of vapor-saturated, silicate melt inclusions. *Journal of Petrology*, 52(12),
1544 2461–2482.
- 1545 Taracsák, Z., Hartley, M., Burgess, R., Edmonds, M., Iddon, F., & Longpré, M.
1546 (2019). High fluxes of deep volatiles from ocean island volcanoes: Insights from
1547 El Hierro, Canary Islands. *Geochimica et Cosmochimica Acta*, 258, 19–36.
- 1548 Teasdale, R., Geist, D., Kurz, M., & Harpp, K. (2005). 1998 eruption at volcán

- 1549 cerro azul, galápagos islands: I. syn-eruptive petrogenesis. *Bulletin of volcanol-*
 1550 *ogy*, *67*(2), 170–185.
- 1551 Thornber, C. R., Orr, T. R., Heliker, C., & Hoblitt, R. P. (2015). Petrologic testa-
 1552 ment to changes in shallow magma storage and transport during 30+ years of
 1553 recharge and eruption at kilauea volcano, hawai ‘i. *Hawaiian Volcanoes: From*
 1554 *Source to Surface*, *208*, 147.
- 1555 Tucker, J. M., Hauri, E. H., Pietruszka, A. J., Garcia, M. O., Marske, J. P., & Trus-
 1556 dell, F. A. (2019). A high carbon content of the hawaiian mantle from olivine-
 1557 hosted melt inclusions. *Geochimica et Cosmochimica Acta*, *254*, 156–172.
- 1558 Tuohy, R. M., Wallace, P. J., Loewen, M. W., Swanson, D. A., & Kent, A. J. (2016).
 1559 Magma transport and olivine crystallization depths in kilauea’s east rift zone
 1560 inferred from experimentally rehomogenized melt inclusions. *Geochimica et*
 1561 *Cosmochimica Acta*, *185*, 232–250.
- 1562 Venugopal, S., Schiavi, F., Moune, S., Bolfan-Casanova, N., Druitt, T., & Williams-
 1563 Jones, G. (2020). Melt inclusion vapour bubbles: the hidden reservoir for
 1564 major and volatile elements. *Scientific Reports*, *10*(1), 1–14.
- 1565 Vinet, N., & Higgins, M. D. (2010). Magma solidification processes beneath ki-
 1566 lauea volcano, hawaii: A quantitative textural and geochemical study of the
 1567 1969–1974 mauna ulu lavas. *Journal of Petrology*, *51*(6), 1297–1332.
- 1568 Wallace, P. J., & Anderson. (1998). Effects of eruption and lava drainback on the
 1569 h₂o contents of basaltic magmas at kilauea volcano. *Bulletin of Volcanology*,
 1570 *59*(5), 327–344.
- 1571 Wallace, P. J., Kamenetsky, V. S., & Cervantes, P. (2015). Special collection:
 1572 Glasses, melts, and fluids, as tools for understanding volcanic processes and
 1573 hazards. melt inclusion co₂ contents, pressures of olivine crystallization, and
 1574 the problem of shrinkage bubbles. *American Mineralogist*, *100*(4), 787–794.
- 1575 Wang, W., Caumon, M.-C., Tarantola, A., Pironon, J., Lu, W., & Huang, Y. (2019).
 1576 Raman spectroscopic densimeter for pure CO₂ and CO₂-H₂O-NaCl fluid sys-
 1577 tems over a wide pt range up to 360 c and 50 mpa. *Chemical Geology*, *528*,
 1578 119281.
- 1579 Whitty, R. C., Ilyinskaya, E., Mason, E., Wieser, P. E., Liu, E. J., Schmidt, A., ...
 1580 others (2020). Spatial and temporal variations in so₂ and pm_{2.5} levels around
 1581 kilauea volcano, hawai’i during 2007–2018. *Frontiers in Earth Sciences*, *8*, 36.

- 1582 Wieser, P. E., Edmonds, M., MacLennan, J., Jenner, F. E., & Kunz, B. E. (2019).
1583 Crystal scavenging from mush piles recorded by melt inclusions. *Nature Com-*
1584 *munications*, *10*(1), 1–11.
- 1585 Wieser, P. E., Edmonds, M., MacLennan, J., & Wheeler, J. (2020). Microstructural
1586 constraints on magmatic mushes under Kīlauea Volcano, Hawaii. *Nature Com-*
1587 *munications*, *11*(1), 1–14.
- 1588 Wieser, P. E., Jenner, F., Edmonds, M., MacLennan, J., & Kunz, B. E. (2020, Au-
1589 gust). Chalcophile elements track the fate of sulfur at Kīlauea Volcano, Hawaii.
1590 *Geochimica et Cosmochimica Acta*, *282*, 245–275. Retrieved from [https://doi](https://doi.org/10.1016/j.gca.2020.05.018)
1591 [.org/10.1016/j.gca.2020.05.018](https://doi.org/10.1016/j.gca.2020.05.018) doi: 10.1016/j.gca.2020.05.018
- 1592 Wright, T. L., & Fiske, R. S. (1971). Origin of the differentiated and hybrid lavas of
1593 Kīlauea Volcano, Hawaii. *Journal of Petrology*, *12*(1), 1–65.